Fundamental Causes of Propagating and Nonpropagating MJOs in MJOTF/GASS Models

Lu Wang and Tim Li

Key Laboratory of Meteorological Disaster, Ministry of Education/Joint International Research Laboratory of Climate and Environmental Change/Collaborative Innovation Center on Forecast and Evaluation of Meteorological Disasters, Nanjing University of Information Science and Technology, Nanjing, China, and International Pacific Research Center, and School of Ocean and Earth Science and Technology, University of Hawai'i at Mānoa, Honolulu, Hawaii

Eric Maloney

Department of Atmospheric Science, Colorado State University, Fort Collins, Colorado

Bin Wang

Key Laboratory of Meteorological Disaster, Ministry of Education/Joint International Research Laboratory of Climate and Environmental Change/Collaborative Innovation Center on Forecast and Evaluation of Meteorological Disasters, Nanjing University of Information Science and Technology, Nanjing, China, and International Pacific Research Center, and School of Ocean and Earth Science and Technology, University of Hawai'i at Mānoa, Honolulu, Hawaii

ABSTRACT

This study investigates the fundamental causes of differences in the Madden–Julian oscillation (MJO) eastward propagation among models that participated in a recent model intercomparison project. These models are categorized into good and poor groups characterized by prominent eastward propagation and nonpropagation, respectively. Column-integrated moist static energy (MSE) budgets are diagnosed for the good and the poor models. It is found that a zonal asymmetry in the MSE tendency, characteristic of eastward MJO propagation, occurs in the good group, whereas such an asymmetry does not exist in the poor group. The difference arises mainly from anomalous vertical and horizontal MSE advection. The former is attributed to the zonal asymmetry of upper-midtropospheric vertical velocity anomalies acting on background MSE vertical gradient; the latter is mainly attributed to the asymmetric zonal distribution of low-tropospheric meridional wind anomalies advecting background MSE and moisture fields. Based on the diagnosis above, a new mechanism for MJO eastward propagation that emphasizes the second-baroclinic-mode vertical velocity is proposed. A set of atmospheric general circulation model experiments with prescribed diabatic heating profiles was conducted to investigate the causes of different anomalous circulations between the good and the poor models. The numerical experiments reveal that the presence of a stratiform heating at the rear of MJO convection is responsible for the zonal asymmetry of vertical velocity anomaly and is important to strengthening lower-tropospheric poleward flows to the east of MJO convection. Thus, a key to improving the poor models is to correctly reproduce the stratiform heating. The roles of Rossby and Kelvin wave components in MJO propagation are particularly discussed.

Corresponding author e-mail: Tim Li, timli@hawaii.edu

1. Introduction

The Madden–Julian oscillation (MJO) is the most prominent mode of intraseasonal variability in the tropics, characterized by an eastward propagating envelope of convective anomalies with a zonal wavenumber 1–3 spatial extent and 30–60-day time scale (Madden and Julian 1972; Weickmann 1983; Murakami and Nakazawa 1985; Lau and Chan 1986). As it modulates deep convection in the tropics, the MJO has large impacts on a variety of weather and climate phenomena across different spatial and temporal scales. For example, it influences the onsets, breaks, and intensity of the Indian and Australian summer monsoons (Yasunari 1979; Wheeler and McBride 2005; Hsu and Yang 2016), the formation of tropical cyclones (Liebmann et al. 1994), and the onset of some El Niño events (Kessler and Kleeman 2000; Chen et al. 2016a,b). Thus, understanding the MJO is of great interest to society.

Current state-of-art global circulation models (GCMs) have limited skill in simulating the MJO (e.g., Slingo et al. 1996; Lin et al. 2006; Kim et al. 2009; Hung et al. 2013). First, eastward propagating signals are not produced in many models. Second, if eastward propagating signals do exist, they often have too weak variance and too fast propagation speed. Third, the spatial structures of the simulated MJOs are often unrealistic. It has also been noted that models that can produce reasonable simulations of the MJO often develop substantial mean state biases (e.g., Kim et al. 2011). As GCMs are essential tools for forecasting weather and projections of future climate, large model deficiencies in representing this dominant mode of atmospheric variability limit our ability to exploit these tools to the greatest extent. Also, this suggests that our understanding of MJO mechanisms is incomplete.

More recently, a multimodel comparison project aimed at understanding models' representation and forecast skill of the MJO has been developed by the Working Group on Numerical Experimentation (WGNE) MJO Task Force (MJOTF) and the GEWEX Atmospheric System Studies (GASS) Panel under the auspices of the Year of Tropical Convection (YOTC) (Petch et al. 2011). An analysis of 20-yr climate simulations from 27 participating models shows that only one-fourth of the models can simulate realistic eastward-propagating MJO-like variability (Jiang et al. 2015). This result implies that even in the latest generation of GCMs, simulating the MJO remains a great challenge. On the other hand, the fact that some models simulated the MJO with fidelity provides us an excellent opportunity to determine what key processes lack realism in the poor group of models. Motivated by this, we would like to address this question: What are the fundamental physical reasons that distinguish the good and poor models in simulating MJO? The

answers to this question are likely to shed light on model improvement and also on understanding the mechanism for eastward propagation of MJO.

A variety of hypotheses have been proposed to explain the eastward propagation of the MJO. Because equatorially trapped Kelvin waves resemble the observed MJO in eastward propagation and many other aspects, early studies proposed that the MJO shares mechanisms with such disturbances (e.g., Lau and Peng 1987; Chang and Lim 1988; Wang 1988; Wang and Rui 1990). However, convectively coupled Kelvin waves typically propagate at a faster speed than the MJO (Wang and Li 2017). A frictional conditional instability of the second kind (CISK) mechanism was proposed as a means to generate an unstable and slow eastward propagating signal. An unstable stratification and moistening to the east of existing MJO convection could provide favorable conditions for new development of cumuli that contribute to the eastward movement of the MJO convective envelope. However, the specific physical processes responsible for moistening to the east of MJO convection remain uncertain and debated. Low-level convergence produced by friction may contribute to moistening east of the convective center. Frictional Kelvin wave–driven vertical moisture advection in the planetary boundary layer (PBL) (Hsu and Li 2012; Liu and Wang 2012; Hsu et al. 2014; Jiang et al. 2015) or vertical transport and detrainment of moisture by shallow cumulus (Johnson et al. 1999) may slowly moisten the lower troposphere prior to an active phase. In recent work viewing the MJO as a moisture mode (e.g., Neelin and Yu 1994; Raymond 2000, 2001; Sobel et al. 2001; Maloney 2009; Sobel and Maloney 2012, 2013), horizontal advection in the free atmosphere is argued to be a more prominent controlling factor for eastward propagation, with possible contributions from synoptic eddies to this moistening. Using this paradigm, surface flux feedbacks have been cited as a hindrance to eastward MJO propagation (e.g., Maloney 2009).

To diagnose the dominant moistening processes that contribute to MJO propagation in moisture mode theory, the column-integrated moist static energy (MSE) budget has been used. This exploits the first-order equivalence between tropical latent heat anomalies and MSE anomalies under conditions of weak tropical temperature gradients (e.g., Sobel and Maloney 2012). The MSE budget is a purely diagnostic analysis and cannot offer definitive causal proof of the processes that control MJO phase speed, but the relationship between the MJO's MSE anomalies and the terms contributing to its tendency can be viewed as suggestive of the MJO's fundamental dynamics. In this study, we will perform an MSE budget of the MJO-like signal for each model and then compare the

TABLE 1. List of models participating MJOTF/GASS project. The good and poor MJO models used for composite in this study are marked by asterisks and hash signs, respectively. (Acronym expansions are available online at http://www.ametsoc.org/PubsAcronymList.)

No.	Institution	Model
1	Centre for Australian Weather and Climate Research	ACCESS
2	Beijing Climate Center (BCC)	BCC AGCM, version 2.1 (BCC-AGCM2.1)
3	Lawrence Livermore National Laboratory	CAM5 with Zhang–McFarlane convection and microphysics for the Cloud-Associated Parameterizations Testbed (CAM5ZMMicroCAPT)
4	Canadian Centre for Climate Modelling and Analysis	CanCM4[#]
5	Climate Prediction Center, NOAA/NCEP	CFSv2 for AMIP (CFSv2AMIP)[#]
6	Centre National de la Recherche Scientifique/Météo-France	CNRM Atmospheric Chemistry Model (CNRM-ACM)
7	Centre National de la Recherche Scientifique/Météo-France	CNRM Atmospheric Model (CNRM-AM)
8	Centre National de la Recherche Scientifique/Météo-France	CNRM-CM*
9	Central Weather Bureau (CWB)	CWBGFS[#]
10	Rossby Centre, Swedish Meteorological and Hydrological Institute	EC-EARTH, version 3 (EC-EARTH3)
11	Environment and Climate Change Canada	Environment Canada Global Environment Model (ECGEM)
12	Academia Sinica	ECHAM5 with snow–ice–thermocline coupler (ECHAM5-SIT)*
13	Institute of Atmospheric Physics, Chinese Academy of Sciences	FGOALS-s2
14	NASA Global Modeling and Assimilation Office	GEOS-5
15	NASA Goddard Institute for Space Studies (GISS)	GISS Model E (GISS_ModelE)*
16	Iowa State University (ISU)	ISUGCM[#]
17	Met Office (UKMO)	Met Office Unified Model (MetUM)
18	Atmosphere and Ocean Research Institute/National Institute for Environmental Studies/JAMSTEC	MIROC5[#]
19	Max Planck Institute for Meteorology	MPI-ESM
20	Meteorological Research Institute	MRI-AGCM*
21	U.S. Naval Research Laboratory	Navy Global Environment Model (NavGEM01)[#]
22	National Center for Atmospheric Research	CAM5
23	Pusan National University (PNU)	PNU Climate Forecast System (PNU_CFS)
24	Colorado State University	Superparameterized Community Atmosphere model, version 3 for AMIP (SPCAM3_AMIP)*
25	George Mason University	Superparameterized Community Climate System Model (SPCCSM)*
26	Texas A&M University (TAMU)	TAMU Community Atmosphere Model, version 4 (TAMU_CAM4)*
27	Scripps Institution of Oceanography	University of California, San Diego (UCSD) Community Atmosphere Model, version 3 (UCSD_CAM3)

composited results for the good and the poor groups; the difference of contributing terms to the MSE tendency between good and poor models may be an essential indicator to help explain model deficiency in the poor group. Jiang et al. (2015) applied the MSE budget in a limited way to the models used here to explain MJO destabilization in good versus bad models.

In section 2, the model data and methods are described. Section 3 compares the MSE budget results for the good and the poor MJO models, and the fundamental causes for the distinctive MSE budget results between the two groups are explored in sections 4 and 5. A discussion is given in section 6 followed by conclusions and a summary in section 7.

2. Data and method

This study analyzes the 20-yr climate simulations from MJOTF/GASS multimodel comparison project (see Jiang et al. 2015). The project consists of a total of 27 models, including both atmosphere-only GCMs (AGCMs) and atmosphere–ocean coupled GCMs. For AGCM runs, weekly sea surface temperatures (SSTs) and sea ice concentrations based on the NOAA Optimum Interpolation SST, version 2, product (Reynolds et al. 2002) during 1991–2010 were specified as the model lower boundary conditions. A list of the 27 models with information including their acronyms and institutions is given in Table 1. To reveal the fundamental cause of different propagation features, the

present study initially focuses on the 13 models that display the highest or lowest skill in simulating eastward propagation of intraseasonal mode. These models were selected by Jiang et al. (2015) by comparing the Hovmöller diagrams of simulated intraseasonal rainfall with the observations. Seven models (CNRM-CM, ECHAM5-SIT, GISS_ModelE, MRI-AGCM, SPCAM3_AMIP, SPCCSM, and TAMU_CAM4) that simulate realistic eastward propagating MJO constitute the good group, and six models (CanCM4, CFSv2AMIP, CWBGFS, ISUGCM, MIROC5, and NavGEM01) that fail to simulate realistic eastward propagation of intraseasonal mode constitute the poor group. Composited results for the good group and the poor group are displayed to reveal the key differences associated with propagation ability. Furthermore, the relationships between possible important process and the modeled eastward propagation skill across all the 27 models are explored by calculating cross-correlation values. Based on the one-tailed Student's t test, a correlation coefficient of 0.32 (0.38) is significant at the 95% (99%) level if the 27 simulations are considered independent.

Observational daily precipitation data were taken from one degree daily (1DD) Global Precipitation Climatology Project (GPCP; Huffman et al. 2001) dataset, version 1.1. Tropospheric winds, temperature, specific humidity, geopotential height, and surface latent and sensible heat fluxes were taken from European Centre for Medium-Range Weather Forecasts (ECMWF) interim reanalysis (ERA-Interim; Dee et al. 2011). Three-dimensional shortwave and longwave radiative heating rate data were from Modern-Era Retrospective Analysis for Research and Applications (MERRA; Rienecker et al. 2011), as they were not provided by ERA-Interim. To verify the consistence of the two reanalysis datasets, we have compared the horizontal patterns of the column-integrated radiative heating rate between MERRA and ERA-Interim; the latter is estimated by shortwave and longwave heat fluxes at the top of atmosphere and at the surface (figure not shown). The period range studied here is 1997–2010. Results obtained from GPCP and the two reanalyses are referred to as observations hereafter. Prior to analysis, all datasets are archived using daily means and horizontal resolution of $2.5° × 2.5°$.

Lag regression against an intraseasonal precipitation index over the eastern Indian Ocean (EIO), which is calculated using 20–100-day bandpass-filtered (Russell 2006) rainfall anomalies averaged over 5°S–5°N, 75°–85°E, is used to extract the dominant intraseasonal mode. All regressed patterns are normalized based on a fixed 3 mm day^{-1} rainfall anomaly in the reference box, following Jiang et al. (2015). By doing so, one may

examine clearly the structure difference between the models and the observation. After deriving the regression patterns for each model, we then take an average for the good and the poor model group respectively to obtain the composite result. Prior to filtering, daily rainfall is subject to removal of the climatological annual cycle. Note that we only focus on boreal winter season (November–April) in this study.

To unveil dynamic causes for distinctive propagating features, we conduct an MSE budget for each model and compare the composite results from the good and the poor MJO groups. MSE m is defined as $m = c_p T + gz + L_v q$, where T is temperature, z is height, q is specific humidity, c_p is the specific heat at constant pressure ($=1004\,\mathrm{J\,K^{-1}\,kg^{-1}}$), g is the gravitational acceleration ($=9.8\,\mathrm{m\,s^{-2}}$), and L_v is the latent heat of vaporization ($=2.5 × 10^6\,\mathrm{J\,kg^{-1}}$). The column-integrated MSE budget can be written following Neelin and Held (1987) as

$$\langle \partial_t m \rangle = -\langle \omega \partial_p m \rangle - \langle \mathbf{V} \cdot \nabla m \rangle + Q_t + Q_r, \qquad (1)$$

where angle brackets represent a mass-weighted vertical integral from the surface to 100-hPa level, p is pressure, $\mathbf{V}$ is horizontal wind vector, and ω is pressure vertical velocity. The lhs term represents MSE tendency, and the first and second terms on rhs represent the vertical and horizontal advection, respectively. Also, Q_t represents the sum of surface latent heat flux and sensible heat flux, and Q_r represents the sum of vertically integrated shortwave heating rate and longwave heating rate. For the observational diagnosis, Q_r is calculated from MERRA and the other terms are derived from ERA-Interim.

3. Column-integrated moist static energy budget

Figures 1a–c show lag–longitude diagrams of regressed rainfall anomalies for the good and poor models as well as the observations. For the good models (Fig. 1b), a robust eastward-propagating intraseasonal mode is visible, which exhibits many similarities with the observations (Fig. 1a). By contrast, no eastward propagation is found in the poor model composite (Fig. 1c), with even hints of westward propagation. The column-integrated MSE anomaly follows the rainfall anomaly closely, consistent with the close correspondence between column humidity and rainfall observed in the tropics (e.g., Schiro et al. 2016). This correspondence suggests that understanding the cause of the different propagation characteristics of the MSE maximum would be useful for understanding the cause of different propagating behaviors of the enhanced rainfall.
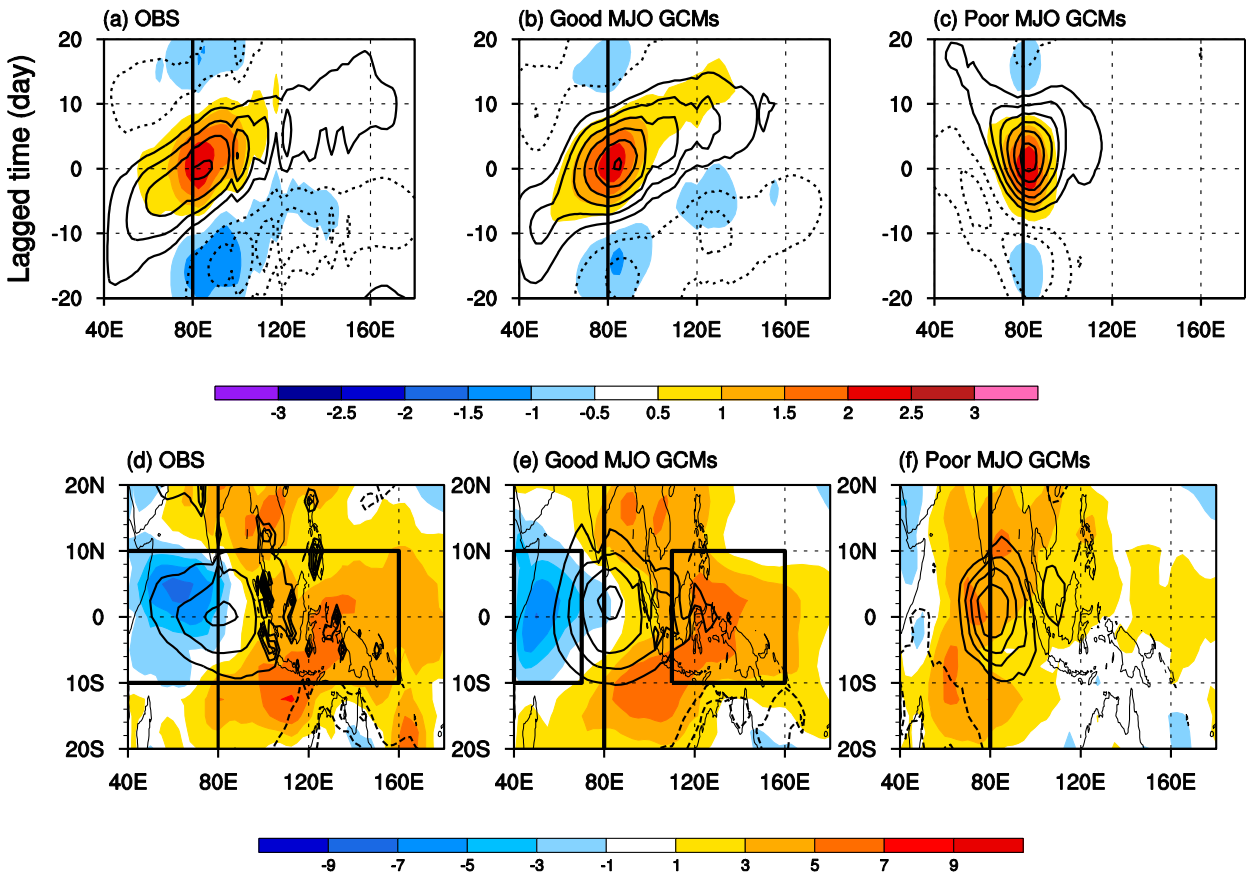
FIG. 1. (a)–(c) Longitude–time evolution of rainfall anomalies (shaded; mm day^{-1}) and column-integrated MSE anomalies (contour; J m^{-2}, contour interval 1×10^{6}, with zero line omitted) averaged over 10°S–10°N by lag regression against 20–100-day bandpass-filtered anomalous rainfall averaged over the equatorial eastern Indian Ocean (5°S–5°N, 75°–85°E). (d)–(f) Regressed day-0 column-integrated MSE tendency anomaly (shaded; W m^{-2}) overlaid by MSE anomaly itself (contour; J m^{-2}; contour interval 2×10^{6}, with zero line omitted). Results are, calculated from (a) GPCP observation and (d) ERA-Interim data or obtained from the (b),(e) good or (c),(f) poor MJO model composite. The rectangle in (d) marks the projection domain 10°S–10°N, 40°–160°E and the rectangles in (e) denote the west box (10°S–10°N, 40°–70°E) and the east box (10°S–10°N, 110°–160°E) discussed in this study.

The horizontal patterns of MSE tendency anomalies (shaded) overlaid by the MSE anomaly (contour) are shown in Figs. 1d–f at lag zero for good and poor MJO models. The good model composite shows positive tendency anomaly to the east of maximum MSE and a negative tendency anomaly to the west. Such asymmetric MSE tendency favors eastward propagation of the MSE maximum. The poor model composite, however, does not have a clear zonally asymmetric MSE tendency distribution. In these poor models, a positive tendency anomaly is observed flanking both sides of the MSE maximum, and the tendency to the west is slightly stronger than that to the east, possibly explaining the hints of westward propagation seen in the poor models in Fig. 1c.

While the above composite results show marked difference in the MSE tendency pattern between the good and the poor MJO models, it is of interest to know

whether the zonal asymmetric MSE tendency pattern could represent the eastward propagation skill in all the 27 models. To address this, we project regressed day-0 column-integrated MSE tendency derived from each model onto the observed regressed column-integrated MSE tendency $\langle \partial_t m \rangle_{obs}$ over 10°S–10°N, 40°–160°E shown in the box of Fig. 1d. The projection coefficient S_x of term x is calculated following Andersen and Kuang (2012) as

$$S_x = \frac{\iint \langle x \rangle \langle \partial_t m \rangle_{obs} \, dA}{\iint \langle \partial_t m \rangle_{obs}^2 \, dA}, \qquad (2)$$

where $\iint dA$ is the integral over 10°S–10°N, 40°–160°E. Here x represents simulated regressed day-0 MSE tendency. If the simulated MSE tendency were the same as
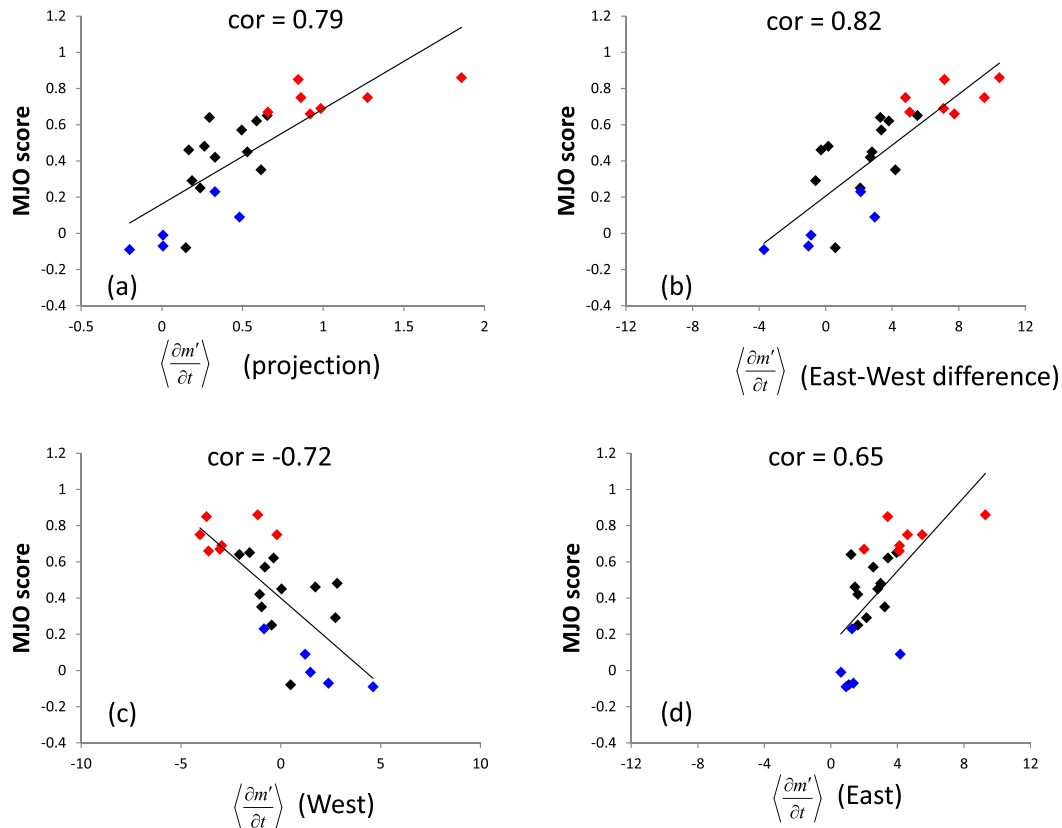
FIG. 2. MJO skill score for eastward propagation over the eastern Indian Ocean (*y* axis) vs (a) projection of column-integrated MSE tendency $\langle \partial m'/\partial t \rangle$ over 10°S–10°N, 40°–160°E; (b) difference of regressed $\langle \partial m'/\partial t \rangle$ between 10°S–10°N, 110°–160°E and 10°S–10°N, 40°–70°E (east minus west); (c) $\langle \partial m'/\partial t \rangle$ average over 10°S–10°N, 40°–70°E; and (d) $\langle \partial m'/\partial t \rangle$ average over 10°S–10°N, 110°–160°E. The MJO skill score is estimated as the PCC between the simulated and observed lag–longitude regression pattern of intraseasonal rainfall over 40°–160°E from day −20 to day +20, but the subregion of 65°–95°E has been removed in the calculation. The good (poor) models used for composite are marked in red (blue). Correlations and least squares fit lines are shown in each panel.

in the observation over 10°S–10°N, 40°–160°E, then S_x would be equal to 1. Thus the projection coefficient can be used to measure the simulation skill of zonally asymmetric MSE tendency pattern. Here *x* could be substituted by other quantities, such as MSE budget terms on right-hand side of Eq. (1). Through this diagnosis, one may measure the fractional contribution of each right hand-side term to observed asymmetric MSE tendency. The reason to use a larger zonally asymmetric domain, compared to Jiang (2017), is because the atmospheric response to a heat source is characterized by a Kelvin wave–like response to the east that extends farther than a Rossby wave response to the west. Observed MSE tendency (Fig. 1d) shows that maximum positive MSE tendency appears over 110°–160°E.

The projection coefficients of MSE tendency in all the 27 models are compared with the MJO eastward propagation skill scores in Fig. 2a. There are two ways to assess the MJO eastward propagation skill using the pattern

correlation coefficient (PCC). One way is to estimate the PCC between the simulated and observed lag–longitude regression pattern of intraseasonal rainfall anomalies from Fig. 1a over entire zonal domain of 40°–160°E from day −20 to day +20. This is essentially same as in Jiang et al. (2015). However, such estimation could not clearly present a significant contrast between the two groups and the poor models with lowest pattern correlations still show high correlation coefficients (0.5–0.6). In the current study, we use another way: when we calculate PCC in the 40°–160°E domain, we remove the subregion 65°–95°E. This is because even poor models can simulate standing oscillations at 80°E, which contaminates the eastward propagation skill score. As is seen, this new PCC metric clearly presents the significant contrast in eastward propagation between the good and the poor models: the former group shows skill scores higher than 0.65, and the latter group shows skill scores lower than 0.25. The contrast is much greater than that shown in Jiang et al. (2015).

Thus, for the remainder of the manuscript, this newly defined PCC-based metric is used as the primary measure of model fidelity for producing realistic MJO eastward propagation. Within the group of poorly skilled models, one model (UCSD_CAM3) is not included in the poor model composite because the good and poor models defined here follows Jiang et al. (2015) based on the average of pattern correlation coefficients calculated at two reference locations, the Indian Ocean (80°E) and western Pacific (150°E).

Figure 2a shows that a high correlation of about 0.8 appears between the MSE tendency projection coefficients and the eastward propagation skills. This indicates that realistic representation of MSE tendency pattern is crucial for a model's ability to simulate MJO eastward propagation. An interesting question is to what extent the zonally asymmetric MSE tendency pattern is contributed by the MSE tendency anomaly in the east side and the west side. To address this question, we separate the projection domain into a west box (10°S–10°N, 40°–70°E) and an east box (10°S–10°N, 110°–160°E) (see rectangles in Fig. 1e), which cover the maximum positive or negative tendency centers. Figure 2b compares the difference of MSE tendency over the east box and the west box (east minus west) with the eastward propagation skill scores across all the models. A high correlation of about 0.8 is produced, which is in agreement with the projection result over the entire domain. Note that significant correlation coefficients appear in both the west box and the east box (see Figs. 2c,d). This suggests that the MSE tendency anomalies in both the east and the west boxes are important in contributing to the zonally asymmetric MSE tendency pattern.

Next, we quantify the relative importance of each MSE budget term at right-hand side of Eq. (1) by calculating the projection coefficient of each term with Eq. (2). A positive projection coefficient suggests that this term contributes positively to observed asymmetric MSE tendency. The composites of projection coefficients for the good and the poor MJO models and their difference are shown respectively in Fig. 3. In the good model composite, the vertical and horizontal advection show positive coefficients with comparable magnitudes, suggesting that they both promote eastward propagation. The terms Q_t and Q_r show negative coefficients, indicating that they hinder the eastward propagation. These results are in good agreement with the observations (Fig. 3a) and previous studies (e.g., Andersen and Kuang 2012). By contrast, the poor group presents negative projections for the vertical advection (Fig. 3c, blue bar) and much weaker projection for the horizontal advection (Fig. 3c, pink bar) compared to the good models. The near-zero projection of MSE tendency (Fig. 3c, black bar) in the poor model composite is
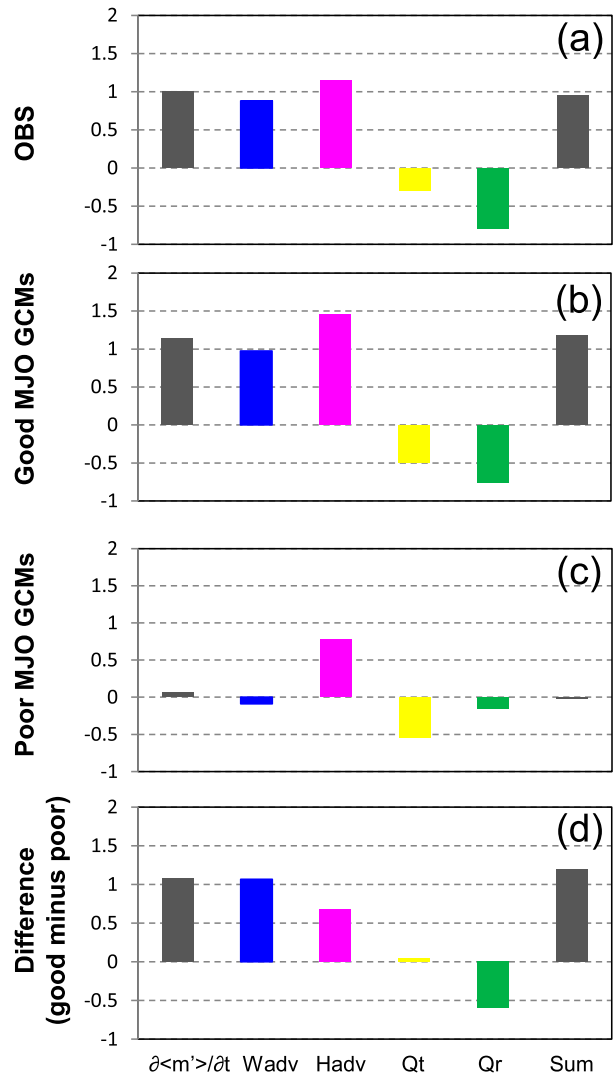
FIG. 3. Projection of the regressed day-0 column-integrated MSE budget terms against the observed MSE tendency anomaly over 10°S–10°N, 40°–160°E. Bars from left to right represent MSE tendency, Wadv, Hadv, Q_t, Q_r, and sum of budget terms (Sum). Results are calculated from (a) reanalysis or from the (b) good or (c) poor MJO model composite. (d) The difference between the good and poor composite results (good minus poor).

thus primarily a consequence of both the reversed sign of vertical advection and the weaker horizontal advection projection. Because of the uncertainty of model parameterizations and dynamical core (e.g., Kiranmayi and Maloney 2011), the MSE budget for both models and observations cannot typically be closed. But the residuals in Figs. 3a–c are quite small, and it gives us confidence to further examine specific processes that contribute to the MSE change.

Figure 3d shows the difference of MSE budget terms between the good and the poor model composites. As
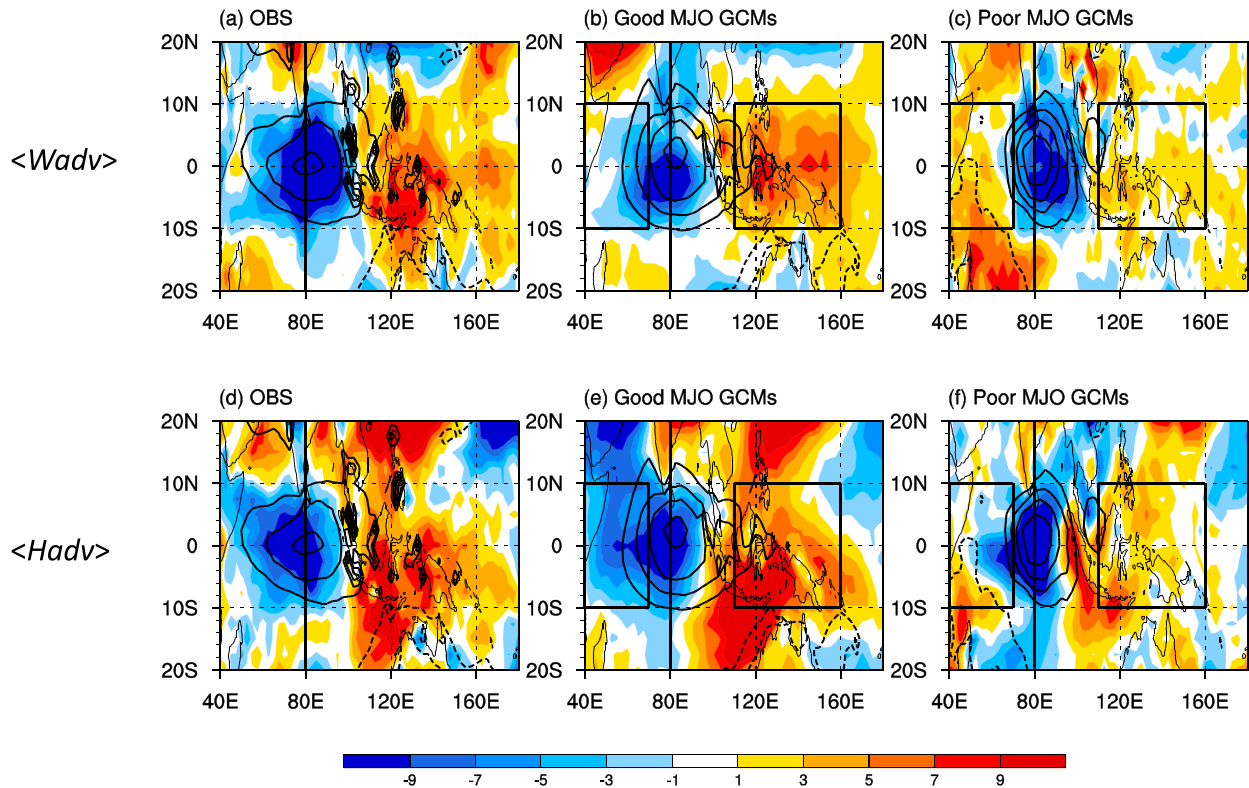
FIG. 4. As in Figs. 1d–f, except that the shading denotes column-integrated (a)–(c) vertical and (d)–(f) horizontal advection of MSE ($W\,m^{-2}$). The rectangles mark the west box ($10°S–10°N, 40°–70°E$) and the east box ($10°S–10°N, 110°–160°E$).

one can see, the difference is primarily attributed to the vertical MSE advection, while the horizontal advection is of the second importance and is about two-thirds of the vertical advection difference. Such a result is confirmed by calculating the east–west difference of each budget term (figure not shown). A further calculation with a reduced latitude range (i.e., $5°S–5°N, 40°–70°E$ and $5°S–5°N, 110°–160°E$) shows essentially the same results (figure not shown). Note that column-integrated vertical advection of MSE would be greatly reduced if a domain with smaller longitude range (e.g., $10°S–10°N, 50°–110°E$) were used (Jiang 2017).

Figure 4 displays horizontal patterns of regressed day-0 column-integrated vertical advection and horizontal advection of MSE for the good and the poor model composites as well as observation. For the vertical advection, the good model group shows apparent zonal asymmetric pattern while the poor model group shows positive anomaly over both the east and west boxes. For the horizontal advection, both the good and the poor model groups have a zonal asymmetric pattern, except that the latter has much weaker amplitude over both sides. This result again suggests that vertical advection difference plays a leading role in the difference between the good and the poor MJO models

while horizontal advection difference plays a second role. Note that one of the good MJO models selected (TAMU_CAM4) has a heavily prescribed diabatic heating profile. To reveal the possible impact of this model on our composite result, we did an additional calculation of the good model composite without this model, and the results are quite similar (figure not shown). Therefore, in the following two sections, the processes responsible for the differing vertical and horizontal MSE advection among good and poor MJO models will be examined in detail.

4. What causes zonally asymmetric vertical MSE advection?

a. Decomposition of vertical advection

To determine the causes of the distribution of the column-integrated vertical MSE advection, we decompose pressure velocity ω and MSE m into low-frequency background state (LFBS; >100 day), intraseasonal (20–100 day), and higher-frequency (<20 day) components such that

$$\omega = \overline{\omega} + \omega' + \omega'' \quad \text{and} \quad m = \overline{m} + m' + m''. \quad (3)$$

West

East
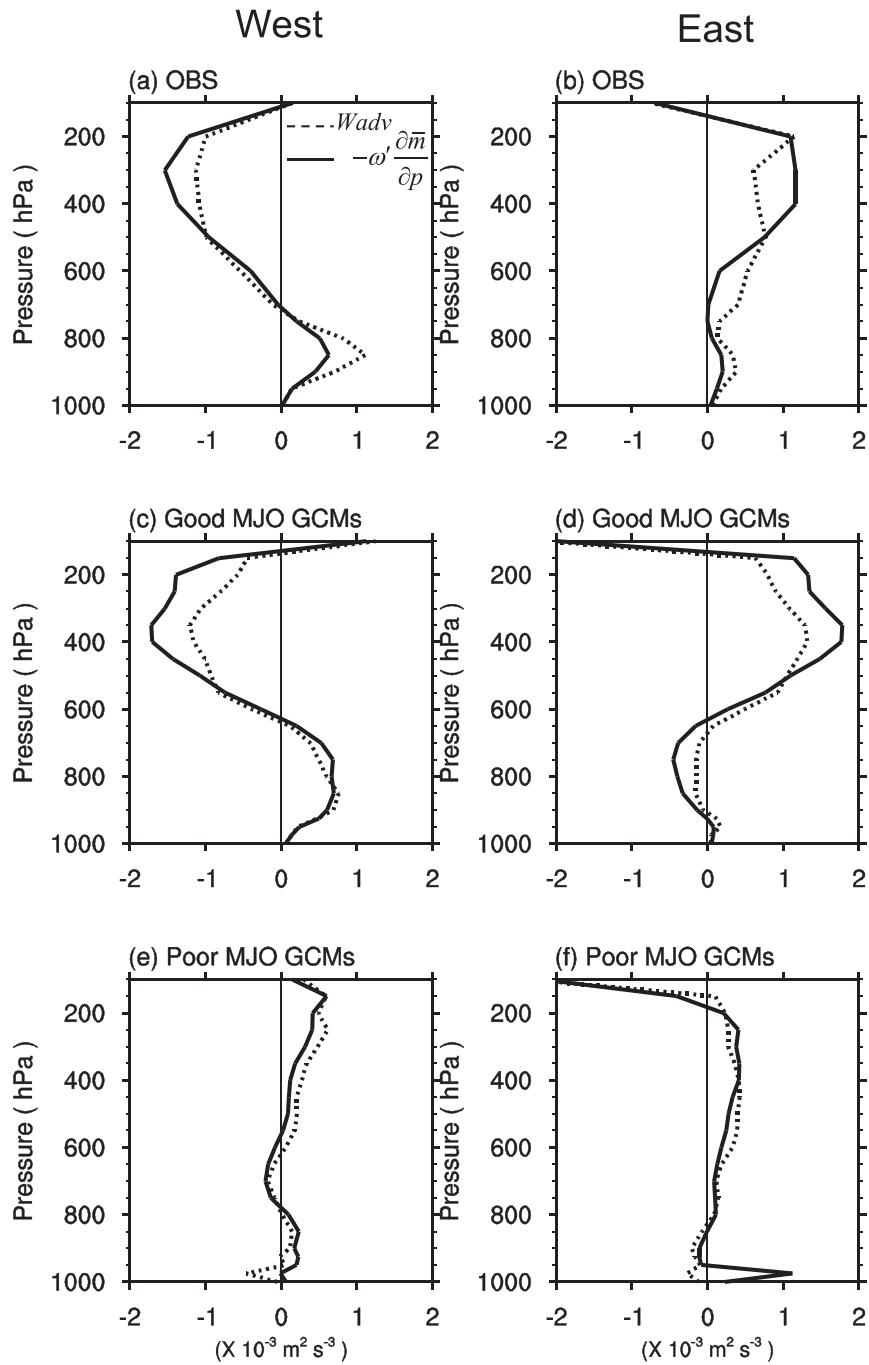
FIG. 5. Profiles of Wadv (dashed) and the component by intraseasonal vertical velocity acting on the mean MSE gradient $-\omega'\partial\overline{m}/\partial p$ (solid) based on (a),(b) reanalysis and the (c),(d) good and (e),(f) poor MJO models composite, for (left) a west box (10°S–10°N, 40°–70°E) average and (right) an east box (10°S–10°N, 110°–160°E) average.

We derive regressed vertical profiles for each model and calculate the ensemble average of profiles over the east box and the west box for the two groups of GCMs. The product of ω and $\partial m/\partial p$ yields nine terms. The profiles of vertical advection of MSE

(Wadv) for the two boxes are both dominated by the component contributed by intraseasonal vertical velocity acting on the mean MSE gradient, $-\omega'\partial\overline{m}/\partial p$. Therefore, we will display only this component and Wadv.

omega
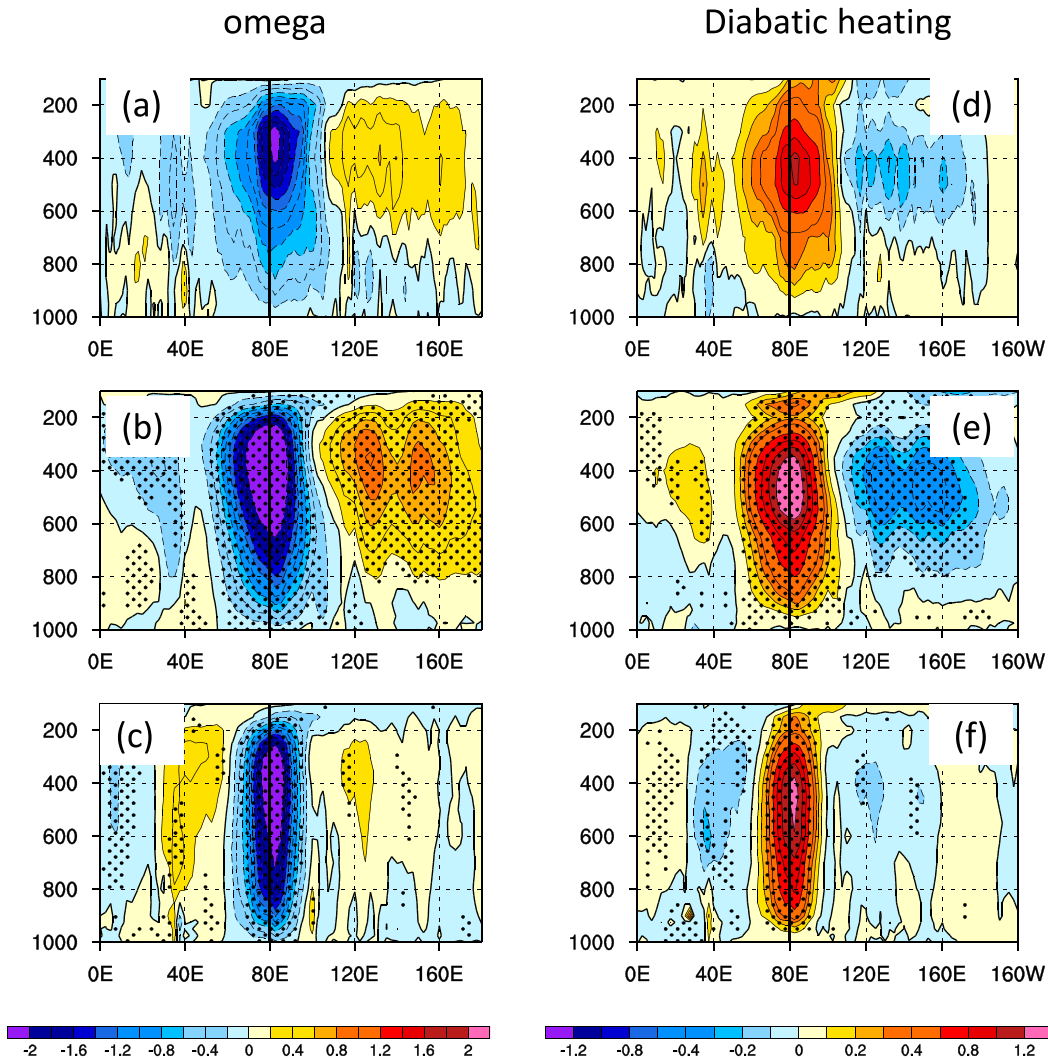
Diabatic heating

FIG. 6. Vertical–longitude cross section of regressed (a)–(c) pressure velocity anomalies (10^{-2} Pa s^{-1}) and (d)–(f) diabatic heating anomalies (K day^{-1}) averaged over 10°S–10°N. Results are based on (a),(d) ERA-Interim or (b),(e) good or (c),(f) poor MJO model composites. For model composite results, the regions passing the 95% significance level are dotted.

Figure 5 shows the profiles of Wadv (dashed lines) and $-\omega'\partial\overline{m}/\partial p$ (solid lines). In observations, Wadv over the east box has two positive peaks (see Fig. 5b): one in the PBL (900 hPa) and the other in the upper troposphere (200 hPa). Note that Wadv over the west box displays an apparent negative peak in upper troposphere and a weak positive peak in PBL (see Fig. 5a). The large zonal asymmetry in Wadv or $-\omega'\partial\overline{m}/\partial p$ is caused by the zonal asymmetry of vertical velocity anomaly, which is characterized by a second baroclinic mode vertical structure. Figures 6a–c show equatorial (10°S–10°N averaged) vertical profiles of regressed pressure velocity anomalies at day 0 (ω'). In the observation (Fig. 6a), an apparent zonal asymmetric pattern relative to the rainfall center (80°E) is visible: downward (upward) anomalies in upper

troposphere (PBL) appear to the east; upward (downward) anomalies in upper troposphere (PBL) appear to the west. The PBL ascent anomaly to the east is associated with boundary layer moisture convergence and shallow convection at the leading edge of MJO convection (e.g., Hsu and Li 2012; Hsu et al. 2014). As the climatological MSE profile minimizes in midtroposphere, both upper-level and lower-level vertical velocity anomalies act to promote a positive column-integrated MSE tendency to the east and a negative column-integrated MSE tendency to the west. Since the vertical velocity anomalies have a top-heavy structure, the upper-level component of Wadv has greater magnitude than the lower-level counterpart and is the main contributor to the vertical integral. A further discussion of the physical
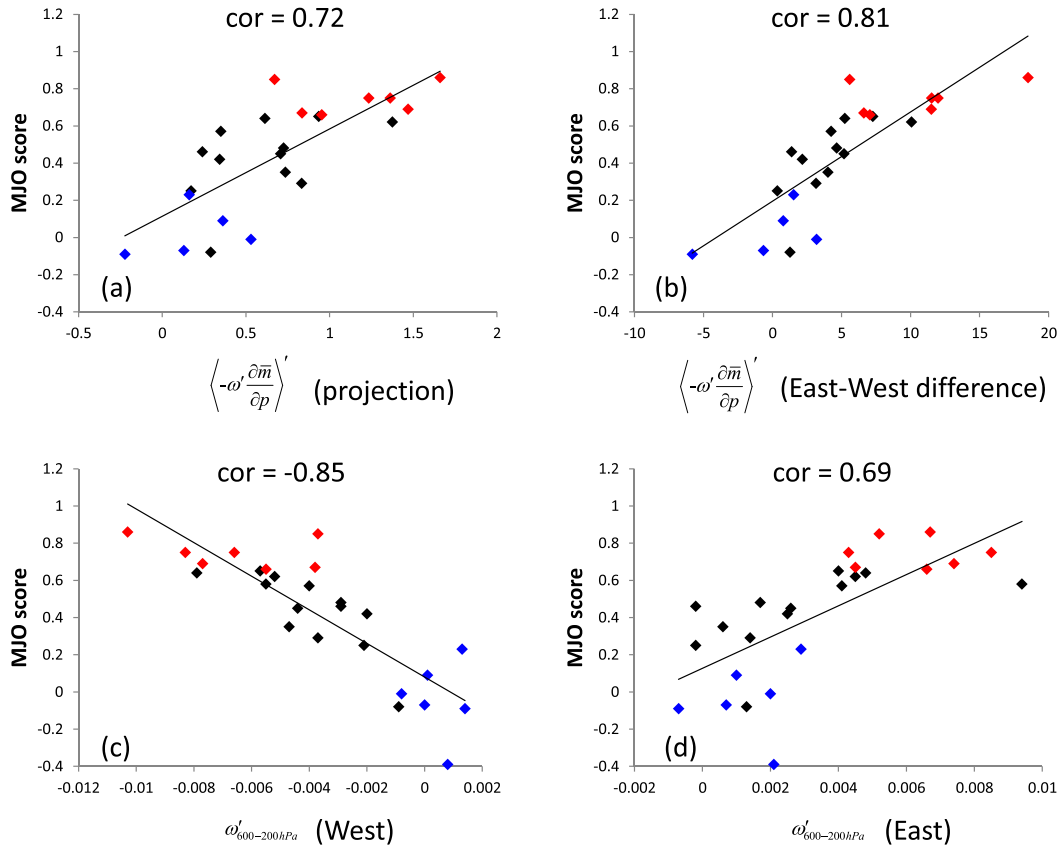
FIG. 7. MJO skill score for eastward propagation over the eastern Indian Ocean (y axis) vs (a) projection of column-integrated vertical MSE advection component $\langle -\omega' \partial \overline{m}/\partial p \rangle$ over 10°S–10°N, 40°–160°E, (b) difference of regressed $\langle -\omega' \partial \overline{m}/\partial p \rangle$ between 10°S–10°N, 110°–160°E and 10°S–10°N, 40°–70°E (east minus west), (c) 600–200-hPa-averaged regressed vertical velocity ω' over 10°S–10°N, 40°–70°E, and (d) 600–200-hPa-averaged regressed ω' over 10°S–10°N, 110°–160°E. The good (poor) models used for composite are marked in red (blue). Correlations and least squares fit lines are shown in each panel.

interpretation of these asymmetric vertical velocity and vertical MSE advection profiles is included in the later part of this section and the discussion section.

The Wadv profiles composited for the good MJO models are generally in agreement with the observations, despite a negative bias in PBL over the east box (see Fig. 5d). This is related to weaker ascent anomaly in PBL at the leading edge of MJO simulated by the good models (see Fig. 6b), suggesting that even the good MJO models have deficiencies in the vertical profiles of vertical velocity. But the zonal asymmetry of Wadv and vertical velocity are apparent in upper troposphere, therefore the zonal asymmetric pattern of column-integrated Wadv in the good model composite is mainly contributed by the upper-tropospheric component (600–150 hPa). By contrast, in the poor MJO model group the east–west contrast of Wadv is not seen (see Figs. 5e,f). The positive anomalies in upper troposphere over the east box are reduced compared to the good group, although the west

box also displays positive anomalies in upper troposphere. It is resulted from the simulated vertical velocity anomalies in the poor model group (Fig. 6c); both sides have weak descent in upper troposphere. Because the mean MSE profiles show little difference between the two groups (figure not shown), the distinctive vertical MSE advection patterns are primarily controlled by different intraseasonal vertical motion (ω') distributions flanking the rainfall center.

Figure 7a compares the projection coefficient of $\langle -\omega' \partial \overline{m}/\partial p \rangle$ with the MJO eastward propagation skill scores in all the models. A high correlation of about 0.7 is produced, indicating that realistic representation of $\langle -\omega' \partial \overline{m}/\partial p \rangle$ is important for a model's ability to simulate MJO eastward propagation. Such a relationship is also observed in the east–west difference of $\langle -\omega' \partial \overline{m}/\partial p \rangle$ (Fig. 7b). As the column-integrated vertical MSE advection is more contributed by the upper level component, the simulated upper-tropospheric

(600–200 hPa) vertical velocity anomaly over the east box and the west box is compared with the eastward propagation skill scores (Figs. 7c,d). The high correlation values (0.7–0.8) demonstrate that the simulated upper-level vertical velocity anomalies play a crucial role in distinguishing the propagation features of the good and the poor models.

b. *Causes of zonally asymmetric vertical velocity in upper troposphere*

Diabatic heating is known to be central to the structure, maintaining and propagation of the MJO (e.g., Mapes 2000; Majda et al. 2007; Kuang 2008; Fu and Wang 2009; Cai et al. 2013). To gain insight into the distributions of the intraseasonal vertical velocity anomalies, the diabatic heating term Q_1 for each simulation is diagnosed as residual of temperature equation as in Yanai et al. (1973). Figures 6d–f show the vertical distribution of regressed diabatic heating anomalies at day 0 for reanalysis and good and poor models. Several aspects are worth noting. First, prominent differences in the zonal extension of maximum heating associated with the intraseasonal deep convection are found between the two model groups. The positive heating anomalies in the good model

composite and the observations span a broad region of around 60° longitude, whereas they have a much narrower zonal width in the poor model composite. Second, an upper-level positive heating to the west of the deep convection, which is likely associated with stratiform clouds (e.g., Lin et al. 2004), is seen in the good model composite and the observations but is absent in the poor model composite. We therefore suspect that a realistic representation of the three-dimensional (3D) diabatic heating structure in the good MJO models may be critical for generating a zonal asymmetric vertical velocity pattern that induces the asymmetric column MSE tendency seen in Fig. 1e.

To assess the hypothesis above, we design a set of numerical experiments using a full-physics atmospheric GCM—ECHAM, version 4.6(Roeckner et al. 1996), at spectral T42 horizontal resolution. Different heating structures are prescribed in sensitivity experiments to understand how the zonal width of the convective heating and stratiform heating in the rear of the MJO contribute to large-scale circulation anomalies. To avoid complicating influences from complex topography, the atmospheric GCM is run on an aquaplanet earth, in which SST distribution is prescribed following the function form (Medeiros et al. 2008):

$$T(\phi) = \begin{cases} 0.5T_{\max}\left[2 - \sin^2\left(\dfrac{3\phi}{2}\right) - \sin^4\left(\dfrac{3\phi}{2}\right)\right], & T(\phi) > 0 \\ 0, & \text{otherwise (high latitudes)} \end{cases} \qquad (4)$$

Here, we set $T_{\max}$ equals to 27°C so SST goes to zero at 60°S and 60°N. The model has no sea ice. Solar irradiance is kept perpetually symmetric about the equator.

We first conducted a control run (CTRL) initiated from a motionless state (4 yr). The remaining experiments with various specified heating anomalies are initialized from the end of CTRL; each run integrates for two years. The three-dimensional heating anomalies are added to the original heating rate in the temperature equation at every time step without interaction with other dynamic or thermodynamic fields (Xiang et al. 2014). In the first sensitivity run (Q_1X) a convective-like positive heating anomaly is placed in the model in the shape of an elongated ellipse centered at 0°, 80°E, which is independent of time (Fig. 8b). It has a central value of 2 K day^{-1} and decreases with distance until it vanishes at an elliptical boundary with a 2000-km east–west semimajor axis and a 1000-km north–south semiminor axis. The amplitude of 2 K day^{-1} is estimated by the observed

one standard deviation of intraseasonal rainfall during boreal winter over the eastern Indian Ocean (6 mm day^{-1}; cf. Fig. 2a in Jiang et al. 2015). In the vertical, the heating assumes a half-sine structure, $\sin(2\pi z/H)$, where H is the total height of the troposphere, and peaks at 500-hPa level (Fig. 8a). This idealized heating forcing is intended to correspond to the narrow and vertically oriented deep convective heating associated with the intraseasonal rainfall in the poor MJO composite (see Fig. 6f). In the second sensitivity run (Q_2X) the prescribed heating is the same as in Q_1X except for a zonal width that is doubled (i.e., 4000-km east–west semimajor axis) (Figs. 8c,d). In the third sensitivity run (Q_str), we add a stratiform-like heating to the west of the convective-like heating in Q_2X. The horizontal pattern of the additional heating has a central value of 1.5 K day^{-1} at 300 hPa. The vertical distribution of the prescribed heating for Q_str is shown in Fig. 8e. This idealized heating profile is intended to correspond to the composited heating

Vertical profile   Horizontal structure
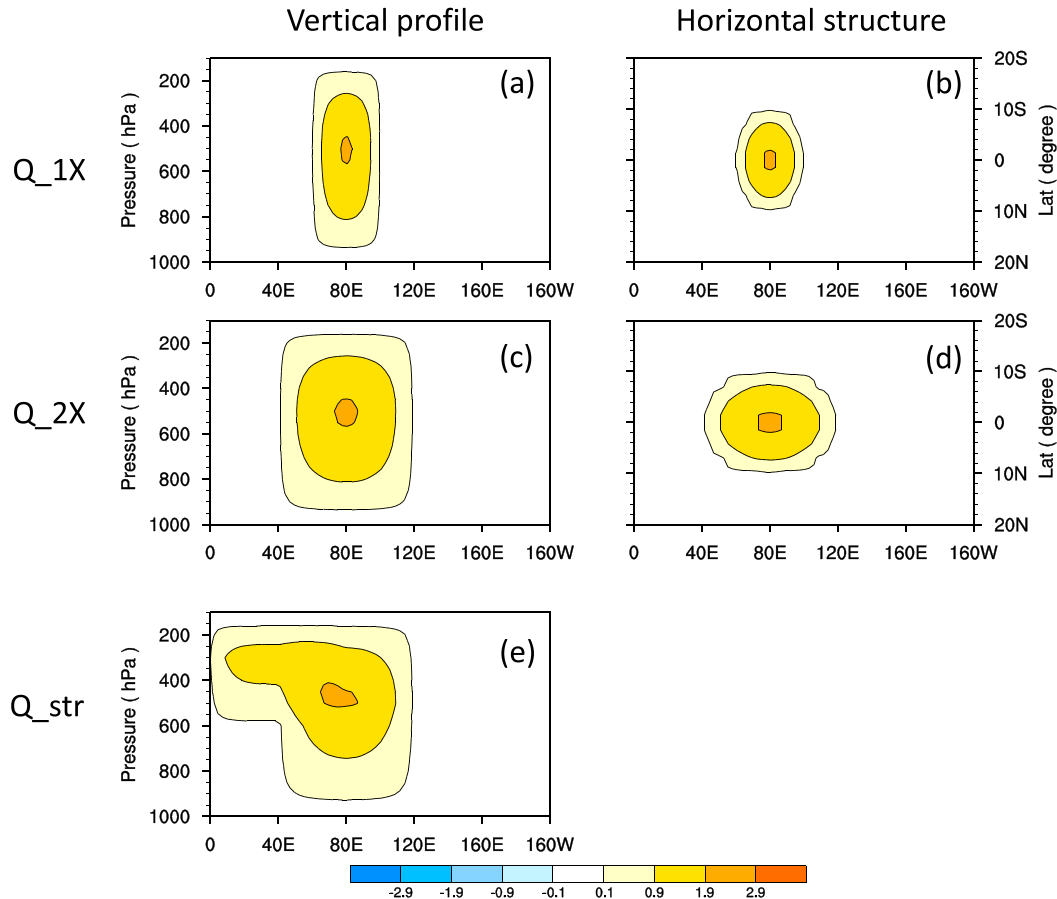
FIG. 8. (a),(c),(e) Vertical profiles and (b),(d) horizontal patterns of prescribed heating anomalies (K day^{-1}) in experiments of (a),(b) Q_1X, (c),(d) Q_2X, and (e) Q_str. In (e), the horizontal pattern of convective-like heating is the same as in (d).

profile in good MJO models (see Fig. 6e). Differences in the mean state of the CTRL and each sensitivity experiment reflect the atmospheric response to the prescribed heating.

Figure 9 displays longitude–height distributions of the vertical motion response to different heating profiles. In response to a narrow heating profile (Q_1X minus CTRL), a prominent upward anomaly at 80°E is produced in the troposphere, which is bracketed to the east and west by modest downward anomalies in upper troposphere (Fig. 9a). It resembles the composite pattern from the poor MJO models (Fig. 6c). When the heating forcing becomes wider, the downward anomalies are substantially enhanced (Fig. 9b). However, widening the convective-like heating does not produce the observed zonal asymmetry structure of the vertical velocity anomalies. When the stratiform-like heating is added to the west of the convective-like heating, ascending flow appears in upper troposphere to the west (Q_str minus CTRL). Moreover, the descent anomaly to the east of

80°E is further enhanced (Fig. 9c). This pattern bears a striking resemblance to that from the good MJO model composite. These model results demonstrate that the existence of the stratiform heating to the west of the MJO rainfall center, rather than the zonal width of the MJO convection region, is responsible for simulating the zonal asymmetry of intraseasonal vertical velocity in upper troposphere (Fig. 9d).

c. A new mechanism for MJO eastward propagation

Based on the MSE budget diagnosis and the numerical experiments above, a new mechanism for MJO eastward propagation is proposed and can be summarized in a schematic diagram (Fig. 10). This mechanism emphasizes the role of the advection of background MSE by second baroclinic mode vertical velocity anomaly. To the east of the MJO convection, a downward anomaly appears in the upper troposphere and an upward anomaly appears in the lower troposphere; to the west, an upward anomaly in association with

FIG. 10. Schematic diagram of a new mechanism for MJO eastward propagation. The cloud describes a gross feature of an MJO that has a deep convective cloud–like structure over a broad region and a stratiform cloud–like structure in the rear in the upper troposphere. The green dashed curves denote climatological MSE profiles. The orange arrows to the east and to the west of the MJO convection region denote the second baroclinic mode vertical velocity anomalies.

stratiform heating appears in the upper troposphere while a downward anomaly appears in the lower troposphere. Given that the background MSE profile minimizes in the midtroposphere, such a distribution of vertical motion anomalies would induce a positive (negative) column-integrated MSE advection to the east (west), promoting eastward propagation of MJO. The existence of the stratiform heating in the rear of the MJO convection is critical in generating zonally asymmetric vertical motion anomalies in upper troposphere, while the PBL process is essential in generating zonally asymmetric vertical velocity anomalies in lower troposphere (Wang and Li 1994; Hsu and Li 2012).

5. What causes distinctions in horizontal MSE advection?

a. Decomposition of horizontal advection

First, the regressed horizontal MSE advection (Hadv) profiles as well as the zonal and meridional components averaged over the east and the west box are displayed in Fig. 11. As expected, a strong east–west contrast of Hadv can be found in the good model composites and in observations (black lines in Figs. 11a–d). The poor model composite, however, exhibits much weaker Hadv to either side of the MSE maximum (Figs. 11e,f). The difference between the good and the poor MJO composites (Figs. 11g,h) shows that the decrease in the zonal asymmetry of Hadv

FIG. 9. Vertical profiles of difference in time-averaged pressure velocity (Pa s^{-1}) along 5°S–5°N between (a) Q_1X, (b) Q_2X, and (c) Q_str and the CTRL run. (d) Domain-averaged pressure velocity anomalies over an east box (orange; 200–600 hPa and 120°E–180°) and a west box (blue; 200–600 hPa and 0°–60°E) [see rectangles in (a)–(c)].

West   East
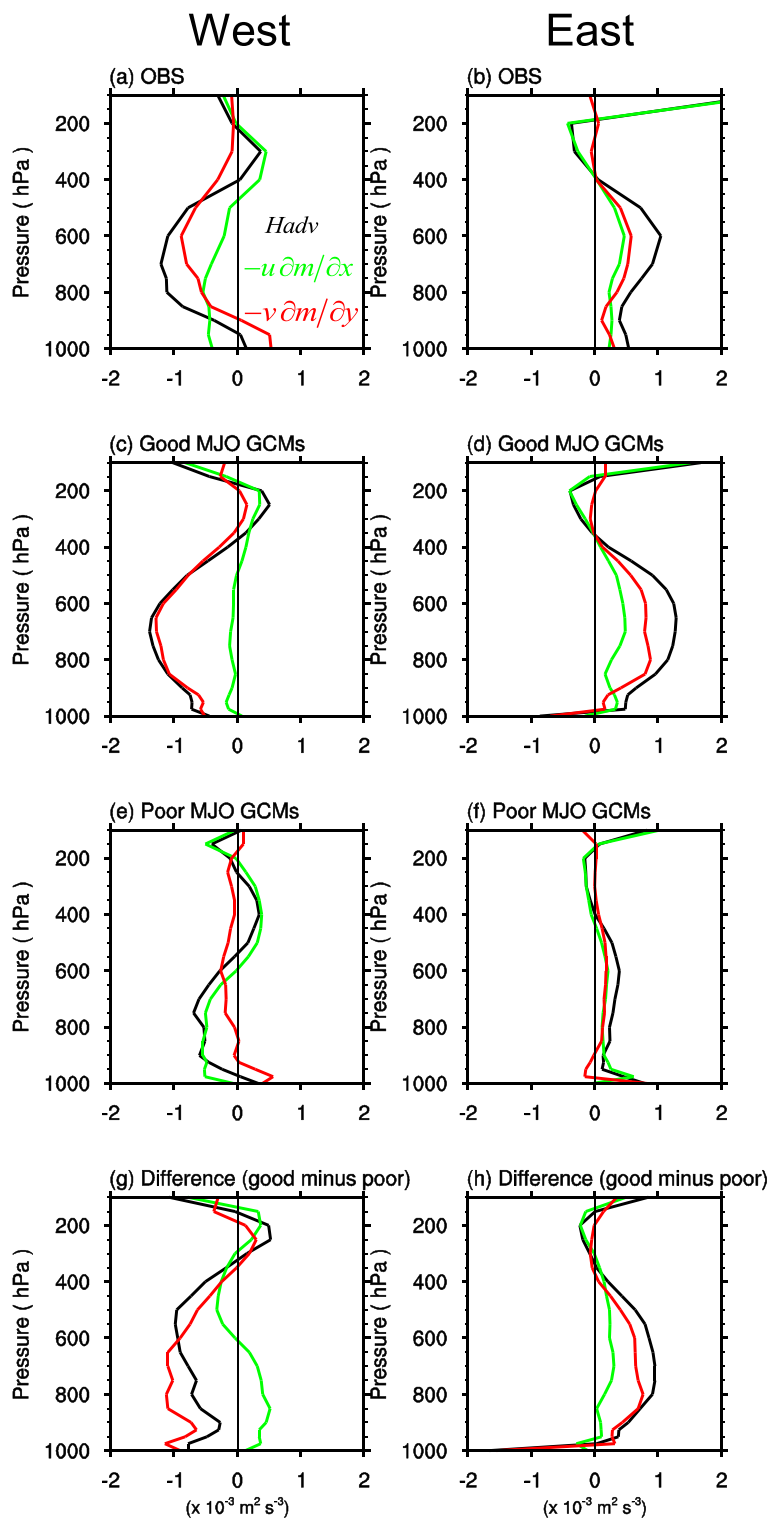
FIG. 11. Profiles of Hadv (black) and its zonal component ($-u\,\partial m/\partial x$; green) and meridional component ($-v\,\partial m/\partial y$; red) averaged over (a),(c),(e),(g) 10°S–10°N, 40°–70°E and (b),(d),(f),(h) 10°S–10°N, 110°–160°E, with values calculated from (a),(b) ERA-Interim data and from the (c),(d) good and (e),(f) poor MJO model composites. (g),(h) The differences between the good and the poor models composites (good minus poor).

(black lines) in the poor group is mainly caused by reduction in the meridional component ($-v \partial m/\partial y$, red lines). The zonal MSE advection, which also contributes to the eastward propagation of the MJO (Liu and Wang 2016), shows less difference between the two model groups (Figs. 11c–f). Kim et al. (2014) argued that meridional MSE advection was an important mechanism for promoting the MJO across the Maritime Continent in observations.

We separate the meridional advection of MSE into moisture, temperature, and geopotential components and find that the meridional MSE advection primarily comes from the moisture component for both groups, in agreement with the weak temperature gradient approximation. The vertical integrated meridional MSE (or moisture) advection in the observation and the good model composite is mainly contributed by the lower troposphere component (see red lines in Fig. 11), while the near-surface component is very weak, consistent with previous studies (e.g., Maloney 2009). Thus, the difference in the vertically integrated horizontal MSE advection between the good and the poor model composites is mainly due to the meridional moisture advection term in the lower free troposphere (600–800 hPa, where maximum anomaly amplitude occurs; see Fig. 11). The cause for such a vertical structure of meridional advection will be further discussed in section 6.

The meridional velocity and moisture are decomposed into LFBS, intraseasonal, and higher-frequency components in the following manner:

$$v = \overline{v} + v' + v'' \quad \text{and} \quad q = \overline{q} + q' + q''. \quad (5)$$

The product of v and $\partial q/\partial y$ thus yields nine components of meridional moisture advection. The primary contributor for the zonal asymmetric meridional advection in the good model composite and the observation is the intraseasonal velocity acting on the LFBS of moisture (i.e., $-v' \partial \overline{q}/\partial y$) (figure not shown). This finding is in agreement with parallel studies by Jiang (2017) and Gonzalez and Jiang (2017). Contributions caused by higher-frequency disturbances (i.e., $-v'' \partial q''/\partial y$) also play a role, consistent with possible modulation by synoptic eddies (e.g., Maloney 2009; Andersen and Kuang 2012). The reduction of the zonal asymmetric pattern in the poor model composite is mainly due to the component $-v' \partial \overline{q}/\partial y$. The result does not change when integrating over 500–800 hPa (figure not shown).

To illustrate the physical mechanism behind the difference in the moisture advection term $-v' \partial \overline{q}/\partial y$ between the good and the poor models, we show the horizontal patterns of intraseasonal wind anomalies and boreal winter mean moisture at 600–800 hPa (Fig. 12). To the east of the enhanced rainfall, the good model composite exhibits pronounced anomalous poleward flow (color shaded). As the mean moisture (i.e., MSE) fields are roughly symmetric about the equator, poleward anomalies induce positive moisture (MSE) advection (Kim et al. 2014). To the west, the good model composite displays equatorward flow. As the mean moisture field attains a maximum south of the equator, the dry advection mainly arises from the Northern Hemisphere, where a strong mean MSE gradient exists. To sum up, the zonal asymmetric distributions of horizontal moisture (MSE) advection in the good MJO models and the observations is caused as follows. To the east, given the symmetric background MSE distribution, poleward flows flanking the equator dominate the positive horizontal MSE advection. To the west, given the asymmetric winter mean MSE distribution, southward dry advection north of the equator dominates the negative horizontal MSE advection.

Marked differences appear in both the anomalous wind and mean moisture field in the poor model composite (Figs. 12e,f). This finding is consistent with a parallel study by Gonzalez and Jiang (2017). In the poor model composite, the poleward flows over the east box and the Northern Hemisphere southward wind over the west box are significantly reduced and the mean moisture near the equator is significantly weaker relative to the good model composite. Therefore, the positive (negative) moisture advection to the east (west) is reduced in the poor model composite. Note that the significant difference of $\partial \overline{q}/\partial y$ over the east and the west box is mainly confined north of the equator (figure not shown). This suggests that the difference in $-v' \partial \overline{q}/\partial y$ mainly arises from the Northern Hemisphere part.

The relationship between the model's fidelity in simulating propagation and the accurate representation of meridional moisture advection term is now explored across all the 27 models (see Fig. 13). A highly significant correlation of about 0.85 is found between the column-integrated meridional MSE advection, whereas only a weak correlation is observed for the zonal advection. This suggests that meridional advection is important for the simulated eastward propagation, while zonal advection is not a good indicator for the MJO propagation skill in a model. Further, the salient fields discussed above such as $-v' \partial \overline{q}/\partial y$, v', and $\partial \overline{q}/\partial y$ over the Northern Hemisphere have significant correlations with the propagation skill scores (see Fig. 14), indicating that the results obtained from the composites are robust across all the models.

b. Causes of poleward wind anomalies east of the convection

It is of interest to understand what causes different magnitudes of poleward wind anomalies to the east of the enhanced rainfall between the two groups, as they
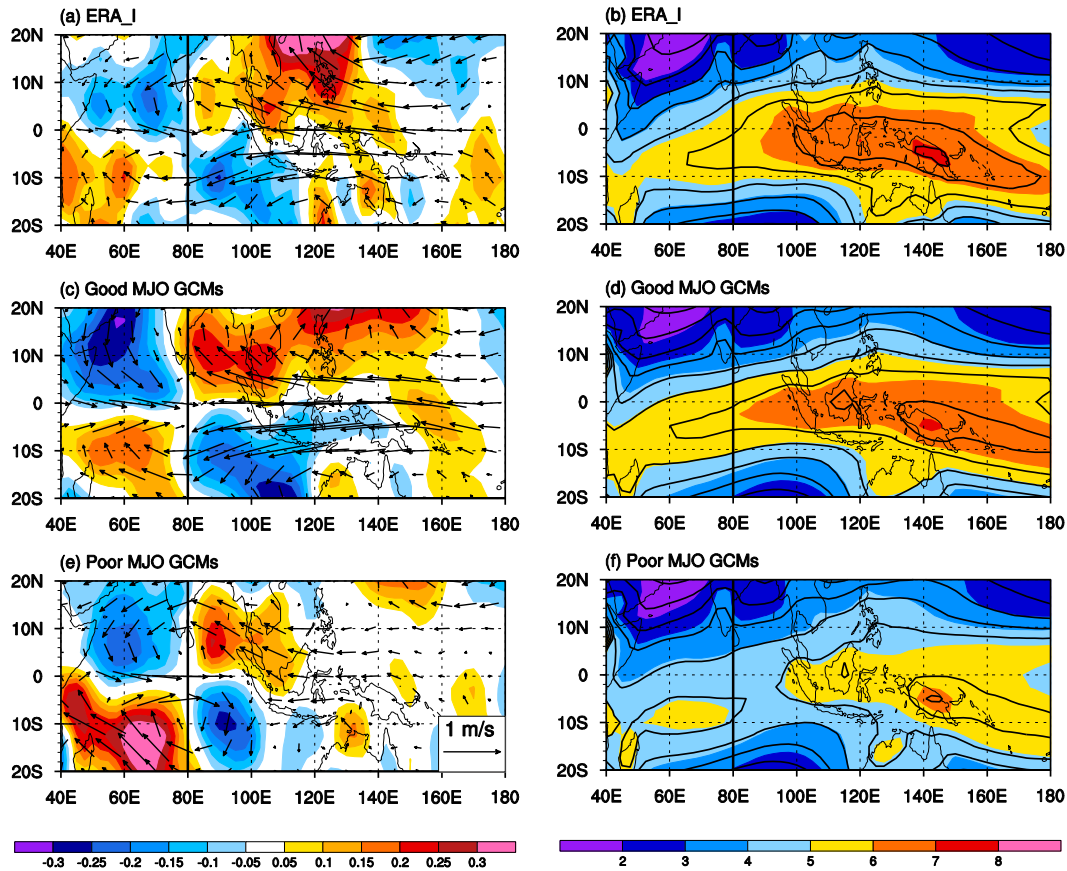
FIG. 12. (a),(c),(e) Horizontal patterns of regressed 600–800-hPa-averaged wind anomalies (vectors; m s^{-1}) and the associated meridional wind component (shaded; m s^{-1}). (b),(d),(f) Horizontal patterns of 600–800-hPa-averaged specific humidity (shaded; g kg^{-1}) and 600–800-hPa integrated MSE (contour; J m^{-2}, contour interval 4×10^6) averaged in boreal winter (November–April). Values are from (a),(b) the ERA-Interim data and the (c),(d) good and (e),(f) poor MJO composites.

are crucial to the magnitude of moisture advection. Does it also relate to the representation of 3D diabatic heating structures? In the observation and the good model composite, negative heating are pronounced over the equatorial western Pacific (see Figs. 6d,e). By contrast, the poor model composite shows only weak negative heating east of the rainfall center (see Fig. 6f). Because poleward flows east of 80°E may be associated with a Rossby wave response to the negative heating at the equator, it is hypothesized that the reduction of poleward flows in the poor MJO models is due to unrealistic representation of the equatorial negative heating, which itself is related to the diabatic heating of the enhanced rainfall region.

To verify the hypothesis, we further diagnose the results from the numerical experiments in section 4b. Figure 15 displays horizontal patterns of the lower-tropospheric wind response and rainfall response to different heating profiles. In response to the narrow convective-like heating forcing, weak suppressed equatorial rainfall and poleward wind anomalies are produced to the east of the enhanced

rainfall (Fig. 15a). The suppressed rainfall and poleward anomalies are enhanced when the convective-like heating is widened (Fig. 15b). After the stratiform-like heating is added, the suppressed rainfall and poleward wind anomalies increase further (Fig. 15c).

These model results suggest that the lower-tropospheric poleward flows to the east of the intraseasonal rainfall center, which are critical to produce positive MSE advection, are related to an anticyclonic Rossby wave response to negative heating anomalies over the equatorial western Pacific Ocean. The stratiform-like heating in the rear of the MJO convection plays a role in enhancing the equatorial negative heating to the east through enhanced zonal-vertical overturning cell and thus it strengthens the lower-tropospheric poleward flow anomaly. To sum up, the different magnitudes of low-level poleward wind anomalies east of the MJO rainfall center between the good and poor MJO models are also due to the simulated stratiform heating. However, the reason for
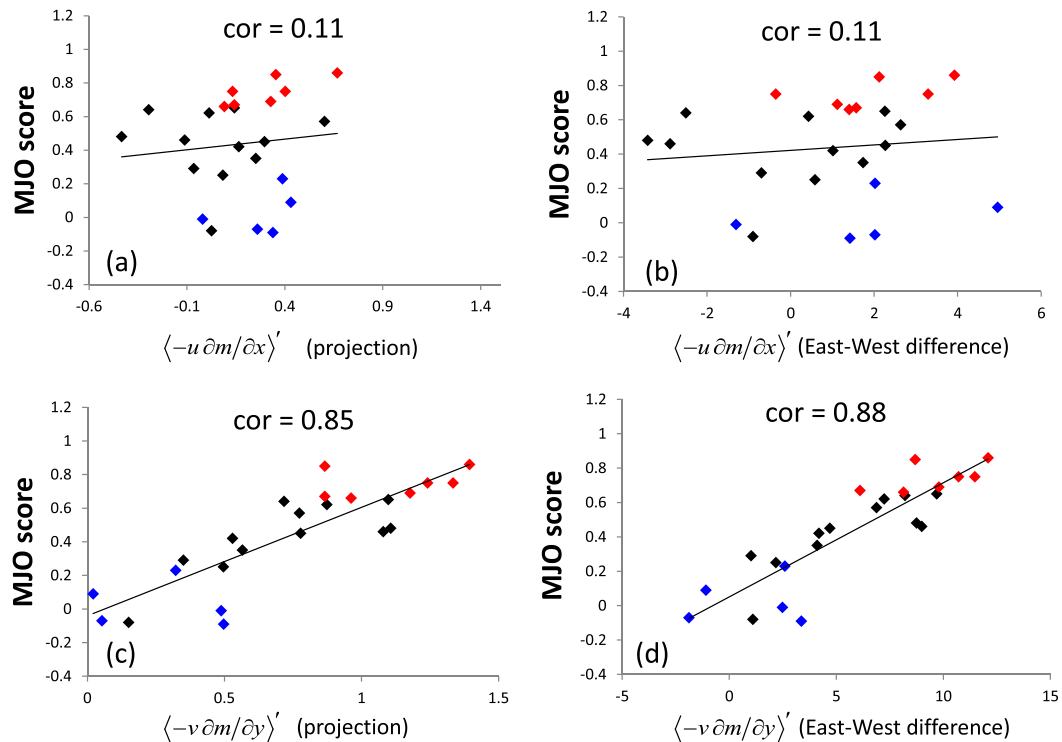
FIG. 13. (a) MJO skill score for eastward propagation over the eastern Indian Ocean (*y* axis) vs projection of the column-integrated zonal MSE advection term $\langle -u \partial m/\partial x \rangle$ over 10°S–10°N, 40°–160°E. (b) As in (a), but for the difference of regressed $\langle -u \partial m/\partial x \rangle$ between 10°S–10°N, 110°–160°E and 10°S–10°N, 40°–70°E (east minus west). (c),(d) As in (a),(b), but for the meridional MSE advection term $\langle -v \partial m/\partial y \rangle$. The good (poor) models used for composite are marked in red (blue). Correlations and least squares fit lines are shown in each panel.

different equatorward wind west of the MJO rainfall in two groups of models, which is asymmetric about the equator, is not clear from these sets of experiments.

c. Key differences of horizontal MSE advection between the good and the poor models

Based on the MSE budget diagnosis and the numerical experiments above, key processes that lead to distinctive horizontal MSE advection between the good and the poor models are summarized in Fig. 16. The first important factor that causes the horizontal MSE advection difference is low-level meridional wind. Because the existence of stratiform heating in the rear of MJO convection in the good model group could enhance upper-level subsidence to the east, the resulting strong negative atmospheric heating could induce strong poleward flows in the lower free atmosphere over the western Pacific Ocean as a Rossby wave response. The good model group also has strong equatorward flows to the west due to the Rossby wave response to MJO convection. Given that background MSE maximizes near the equator to the east, whereas it peaks in the Southern Hemisphere to the west, such a circulation pattern results in apparent positive (negative) horizontal advection to the east (west) and

contributes to the zonally asymmetric MSE tendency. By contrast, the poor model group has weaker poleward flows to the east and weaker southward flow in the Northern Hemisphere to the west. The second important factor is the mean state difference between the good and the poor models. The mean moisture gradient near the equator is significantly weaker in the poor model group. As a result, even the same anomalous meridional flow would lead to weaker MSE advection. To sum up, both the meridional component of intraseasonal flows in the lower free atmosphere (primarily the first baroclinic mode low-level circulation anomaly) and the low-level mean moisture field contribute to the differences in horizontal MSE advection between the good and the poor model group and thus their eastward propagation characteristics.

6. Discussion

a. Role of the Rossby wave component in MJO eastward propagation

So far there are two schools of thinking regarding the role of the Rossby wave component of MJO flows in MJO eastward propagation. One school of thought argues that a stronger Rossby wave component slows down
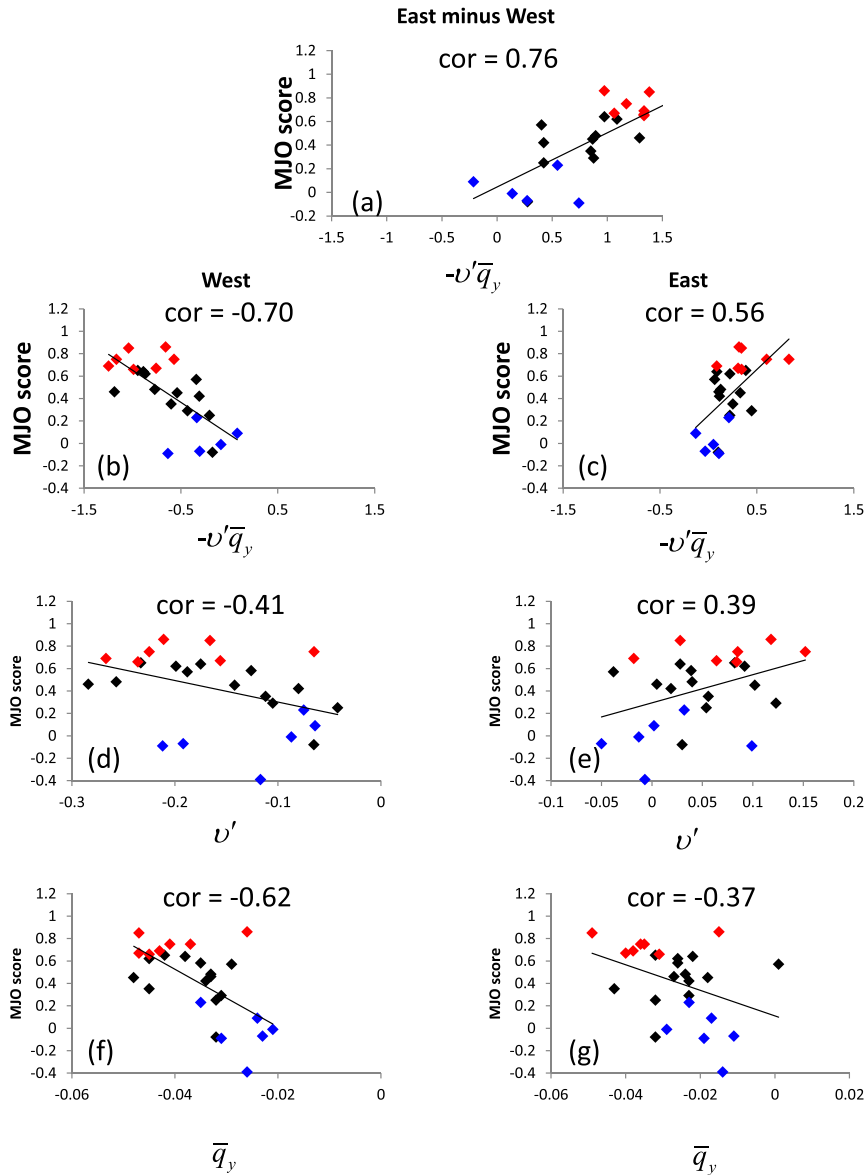
FIG. 14. MJO skill score for eastward propagation over the eastern Indian Ocean (y axis) vs regressed 600–800-hPa-averaged meridional moisture advection term $-v'\overline{q}_y$ and its components (x axis). (a) Zonal asymmetric $-v'\overline{q}_y$, which is obtained by difference of the east region–averaged value and the west region–averaged value (east minus west). Here the east region is defined as 0°–10°N, 110°–160°E, and the west region is defined as 0°–10°N, 40°–70°E. The west region–averaged variables of (b) $-v'\overline{q}_y$, (d) v', and (f) $\overline{q}_y$. (c),(e),(g) as in (b),(d),(f), but for the east region–averaged variables. The good (poor) models used for composite are marked in red (blue). Correlations and least squares fit lines are shown in each panel.

the MJO eastward propagation as the Rossby wave tends to propagate westward. By comparing near-surface (925 hPa) wind anomalies associated with the normalized MJO rainfall, Jiang et al. (2015) noted that the poor model composite displays a stronger Rossby wave component compared to the good model composite (see Fig. 15 of Jiang et al. 2015). This prompted Jiang et al.

(2015) to hypothesize that a stronger Rossby wave component might hinder eastward propagation. Another school of thought argues that a stronger Rossby wave component favors eastward propagation because equatorward meridional wind anomalies associated with the Rossby wave would promote negative MSE advection to the west by advecting drier and colder air from

(a) Pr (Q_1X - ctrl)

(b) Pr (Q_2X - ctrl)

(c) Pr (Q_str - ctrl)

(d)
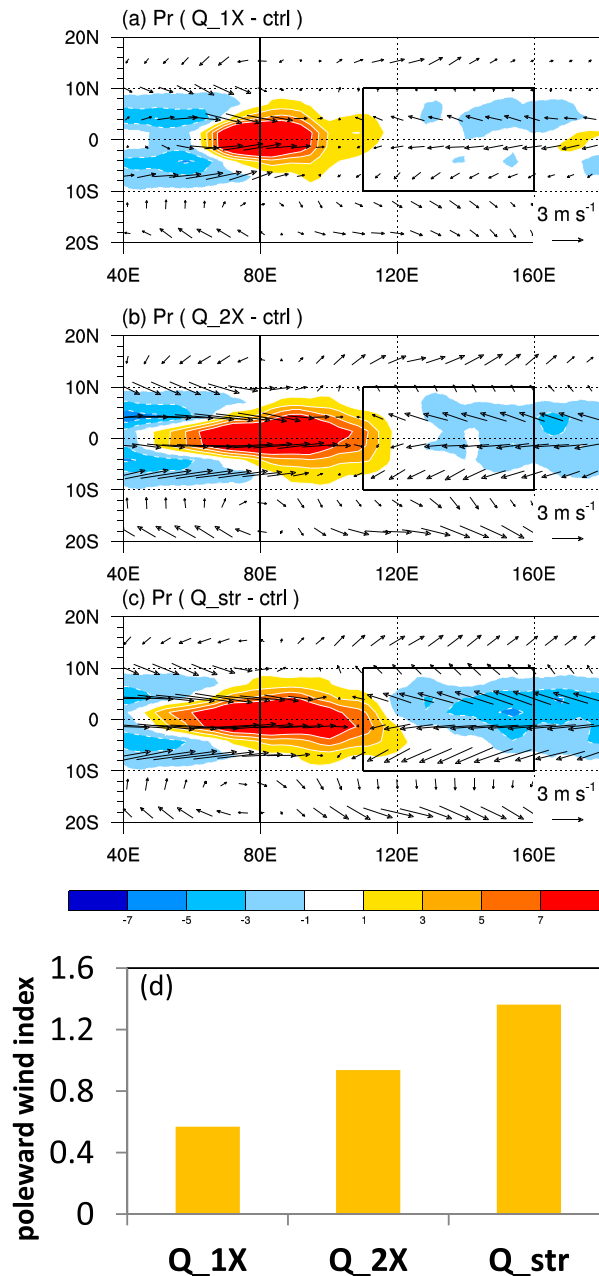
FIG. 15. Horizontal patterns of difference in time-averaged rainfall (shaded; mm day^{-1}) and 700-hPa wind (vectors; m s^{-1}) between (a) Q_1X, (b) Q_2X, and (c) Q_str and the CTRL run. (d) The bars denote poleward wind index (m s^{-1}) calculated by meridional wind over 10°S–10°N, 110°–160°E [see rectangles in (a)–(c)].

off-equatorial regions (Sobel et al. 2014), which enhances the zonal asymmetry of the MSE tendency.

One mystery is why a stronger 925-hPa Rossby wave component in the poor model composite corresponds to a weaker horizontal advection in the west, compared to that in the good model composite. As revealed
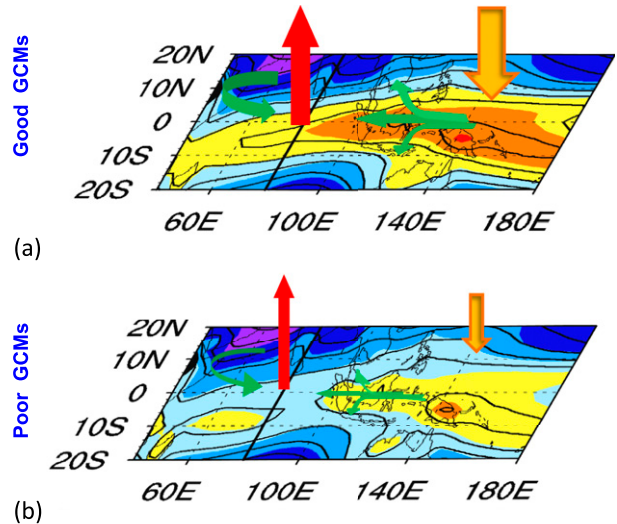
FIG. 16. Schematic representation of the key processes for different horizontal MSE advection between (a) the good and (b) the poor MJO model composites. The horizontal maps denote the distributions of boreal winter mean humidity (MSE) averaged over 600–800 hPa (as in Figs. 12d,f). The green arrows denote the key anomalous flows in the lower free atmosphere that induce positive (negative) MSE advection to the east (west). The red arrows at 80°E denote positive heating associated with MJO deep convection, whereas the orange arrows over the western Pacific Ocean denote negative heating in association with anomalous subsidence.

in Fig. 11a, the observed negative meridional MSE (moisture) advection in the west is confined over lower troposphere (600–800 hPa) while the near-surface level has much weaker amplitude. This suggests that when diagnosing the role of anomalous circulation to moisture advection, one should focus on the lower free troposphere rather than that near the surface. Recall that the 600–800-hPa-averaged intraseasonal wind in the good model composite shows stronger equatorward wind over the Northern Hemisphere to the west of the MJO rainfall center compared to the poor model composite (see Figs. 12c,e). This indicates that the good models exhibit a stronger Rossby wave component. This in-phase relationship is further validated by the relationship of the simulated Rossby wave strength (i.e., regressed westerly anomaly over 5°S–5°N, 40°–70°E or the regressed southward wind anomaly over 0°–10°N, 40°–70°E at 600–800 hPa and the MJO eastward propagation skill score (Figs. 17a,b). A significant correlation (magnitude of about 0.4) is observed between the lower-tropospheric Rossby wave strength and the MJO scores. In contrast, an insignificant correlation is found between the 925-hPa Rossby wave strength and the eastward propagation scores (Figs. 17c,d).
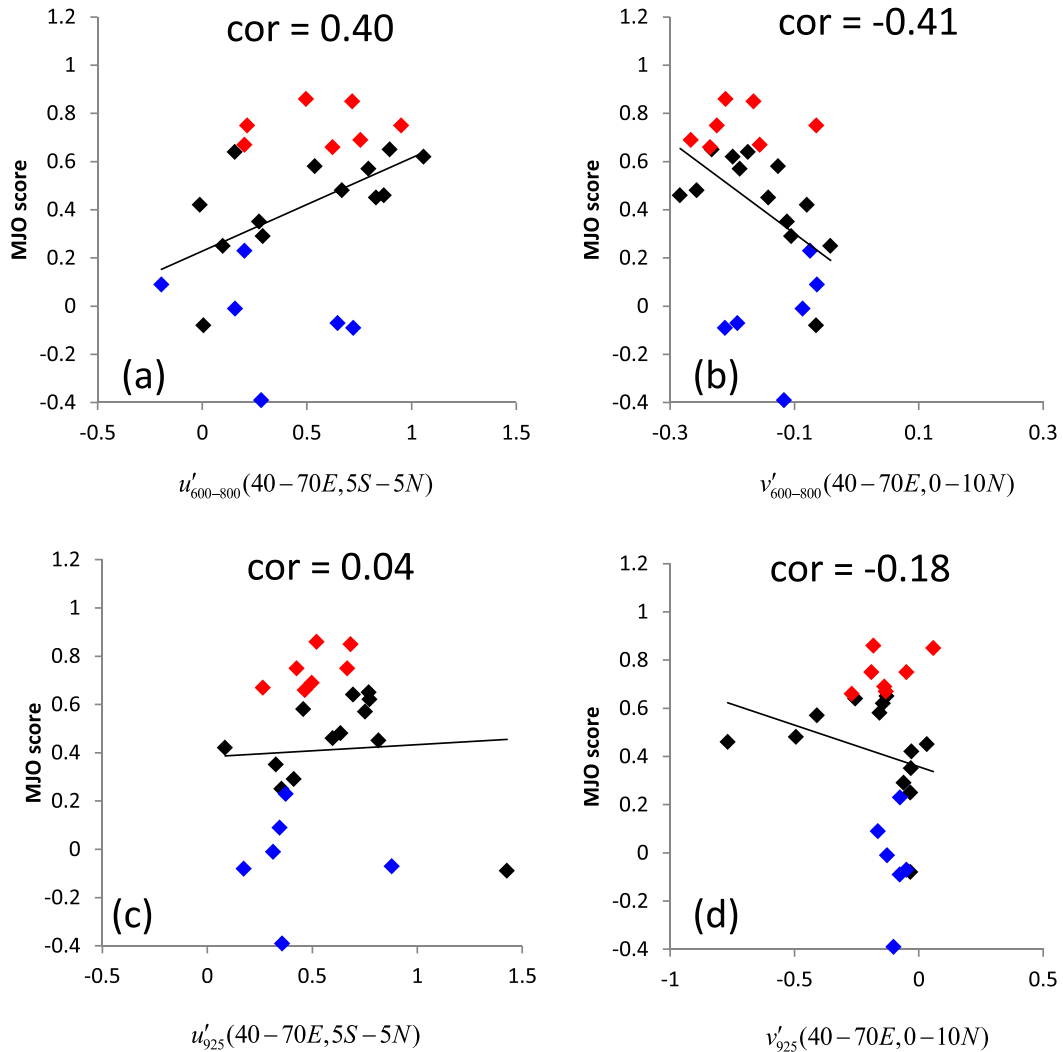
FIG. 17. (a) MJO skill score for eastward propagation over the eastern Indian Ocean (*y* axis) vs the regressed intraseasonal zonal wind anomaly averaged over 600–800 hPa in 5°S–5°N, 40°–70°E. (b) As in (a), but for the meridional wind anomaly in 0°–10°N, 40°–70°E. (c),(d) As in (a),(b), but at 925 hPa. The good (poor) models used for composite are marked in red (blue). Correlations and least squares fit lines are shown in each panel.

An interesting question is why the meridional moisture advection by near-surface flow is weaker than that by lower-tropospheric flow? To address this question, we compare the composited wind anomalies at 925 and 700 hPa (Fig. 18). As one can see, the southward anomaly over the region 0°–10°N, 40°–70°E at 925 hPa is in general weaker than that at 700 hPa. The weaker southward wind at 925 hPa is due to a couple of factors: 1) stronger damping in PBL and 2) an eastward shift of near-surface convergent flow to the convective center near 80°E. The latter is a response to the low pressure anomaly associated with the MJO convection at top of PBL. In contrast, the 700-hPa wind has a typical free-atmosphere Rossby wave gyre structure in response to the midtropospheric heating,

with equatorward flow around 60°E and poleward flow at 80°E.

b. Role of the Kelvin wave component: Meridional versus zonal wind anomaly

It has been shown that the Kelvin wave response to diabatic heating tends to promote eastward propagation as it induces the PBL convergence and moistens the lower troposphere to the east (Hsu and Li 2012; Jiang et al. 2015). As shown in Fig. 18, the equatorial easterly anomaly to the east of the convection is stronger in the good model composite than in the poor model composite at both 700 and 925 hPa. A high positive correlation of about 0.7 is found between the Kelvin wave strength (i.e., regressed easterly anomalies over 5°S–5°N,
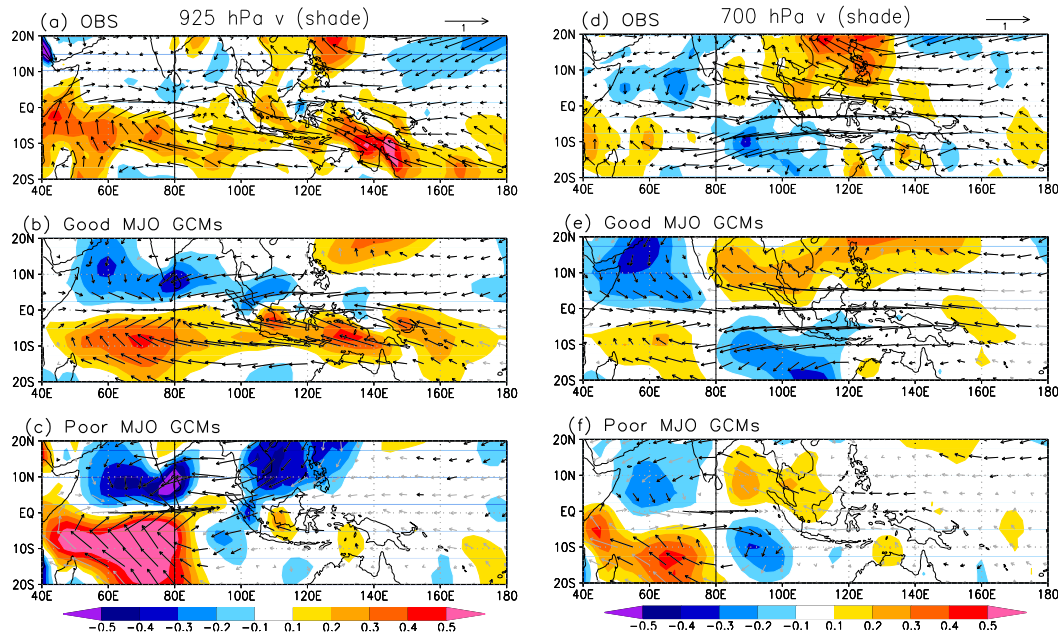
FIG. 18. (a)–(c) Horizontal patterns of regressed 925-hPa wind anomalies (vectors; m s^{-1}) and the associated meridional wind component (shaded; m s^{-1}). (d)–(f) As in (a)–(c), but for 700-hPa wind anomalies. Values are from (a),(d) the ERA-Interim data and the (b),(e) good and (c),(f) poor MJO composites. In (b),(c),(e),(f), regions where composite wind anomalies are significant at 95% level are denoted by black vectors.

110°–160°E and the MJO propagation score (see Fig. 19a). However, such a zonal wind difference plays little role in causing MSE tendency difference, because the zonal MSE (or moisture) advection does not contribute to the overall MSE tendency difference between the good and the poor models (see Fig. 11h). In fact, little correlation exists between the zonal advection and the MJO propagation score for all the 27 models (see Figs. 13a,b). The cause of this is the weak background zonal MSE/moisture gradient over the Maritime Continent and the western Pacific.

As revealed by the MSE budget analysis, the meridional component (i.e., $-v'\partial\overline{q}/\partial y$) in lower troposphere, especially the Northern Hemisphere part, is the main contributor to the horizontal advection. The good relation between the equatorial zonal wind and the eastward propagation score shown in Fig. 19a is attributed to the fact that the former is closely linked to poleward flows in lower troposphere. The poleward anomaly to the east of the MJO convection is a result of Rossby wave response to a negative heating anomaly over the equatorial western Pacific Ocean, associated with compensating subsidence east of the MJO convection. In other words, enhanced negative heating associated with the zonal-vertical overturning cell to the east results in both stronger poleward flows and easterly anomalies. A significant correlation of 0.65 is found between the MJO skill score and the strength of the negative heating (Fig. 19b).

A marked difference in meridional flows is found between 700 and 925 hPa in the east box (Fig. 18). The former is poleward while the latter is equatorward. This implies an opposite meridional MSE advection between the two levels. The former is a direct free-atmosphere Rossby wave response to the negative heating in front of MJO convection. The latter is more influenced by convergence in PBL in response to the low pressure anomaly in the lower troposphere associated with Kelvin wave response. As poleward (equatorward) flows induce positive (negative) MSE advection, the positive MSE horizontal advection to the east is primarily contributed by the lower free–troposphere flow rather than the near-surface flow (Fig. 11).

c. Relative roles of vertical MSE advection and atmospheric radiative heating

The MSE budget diagnosis above suggests that vertical MSE advection plays an important role in generating the zonal asymmetric MSE tendency, while atmospheric radiative heating Q_r plays an opposite role. Under the weak temperature gradient approximation in the tropics, the vertical advection of dry static energy $(c_pT + gz)$ is nearly balanced by atmospheric diabatic heating Q_1 (see Figs. 20a–c). This implies that part of vertical advection of moist static energy $(c_pT + gz + L_vq)$ could be offset by Q_r, and the resulting MSE tendency in the column integral taking this cancellation into
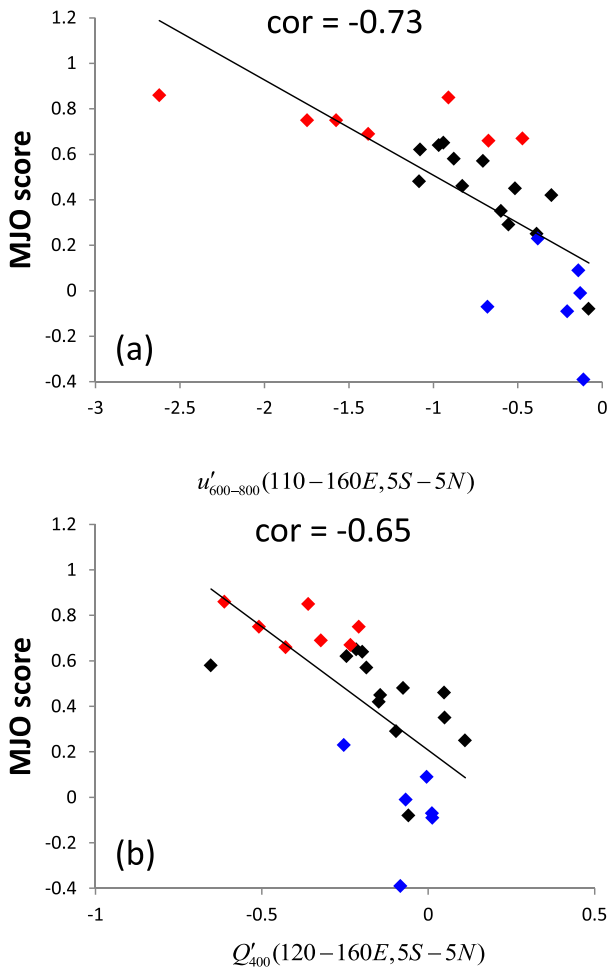
FIG. 19. (a) MJO skill score for eastward propagation over the eastern Indian Ocean (*y* axis) vs regressed day-0 zonal wind anomaly at 700 hPa averaged over 5°S–5°N, 110°–160°E. (b) As in (a), but for intraseasonal atmospheric heating Q_1 at 400 hPa averaged over 5°S–5°N, 120°–160°E. The good (poor) models used for composite are marked in red (blue). Correlations and least squares fit lines are shown in each panel.

account becomes equivalent to a moisture tendency under weak temperature gradient considerations. [Figures 20d–f](#) display the vertical profiles of sum of Wadv and Q_r (red) as well as Wadv itself (black). It is seen from the observations that even adding the Q_r effect, the column-integrated vertical MSE advection over the east box still shows a positive tendency, consistent with that implied by [Fig. 3](#). Over the west box, the negative anomaly of Wadv dominates the Q_r effect above 600 hPa while the positive anomaly of Wadv in lower levels is associated with upward moisture transport near the MJO convective center (note that the eastern edge of the west box is close to the main MJO convective center). In the good model composite, the vertical profiles are in general similar to the observations, except that a negative bias of

combined Wadv and Q_r appears in the east box in lower troposphere. This is mainly due to a deficiency in simulating Wadv in the good models (see [Fig. 5d](#)). Therefore, the zonal asymmetric distribution of vertical MSE advection dominates the Q_r effect. These results confirm that even when considering radiative heating anomalies, Wadv is still an important factor that distinguishes the good and the poor models. One further cautionary point on [Figs. 20d–f](#) is that the sum of Q_r and Wadv should not necessarily be interpreted as a moistening anomaly at an individual level, only in the column integral. Transport due to eddy flux convergence is an important means of vertical redistribution that transports humidity between levels.

7. Conclusions

In this study, we examined key physical mechanisms for eastward propagation of the MJO with the multimodel database from MJOTF/GASS. First, we analyzed 13 representative models categorized into good and poor groups based on their simulation of MJO propagation according to [Jiang et al. (2015)](#); seven models produce realistic eastward propagation (good group) and six models only have stationary intraseasonal rainfall (poor group). The comparison of the good and the poor groups' composite results are used to identify the key processes for the MJO eastward propagation. Then, we compared MJO skill scores for eastward propagation over the eastern Indian Ocean and possible important processes by using all the 27 models. The MJO skill score is estimated based on the pattern correlation coefficient (PCC) between the simulated and observed lag–longitude regression pattern of intraseasonal rainfall anomaly over 40°–160°E from day −20 to day +20, with the reference region 65°–95°E removed. This newly defined PCC metric clearly presents the significant contrast of propagation behaviors between the good and the poor models.

The column-integrated MSE budget is examined for each model, and the composited results for each group are used to understand the different propagating features. In the good group, eastward propagation is caused by the combination of realistic vertical advection and horizontal advection; these models produce a positive MSE tendency to the east of enhanced rainfall and negative tendency to the west. In the poor group, a strong east–west contrast in MSE tendency is not present. Vertical advection is identified as the main contributor to the MSE tendency distribution, and horizontal advection has a magnitude about a third smaller.

Decomposition of vertical advection anomalies reveals that they are mainly due to intraseasonal vertical

$$-\omega\partial\left(c_p T + gz\right)\big/\partial p$$

$$-\omega\partial\left(c_p T + gz\right)\big/\partial p + Q_1$$

$$-\omega\partial m/\partial p$$

$$-\omega\partial m/\partial p + Q_r$$
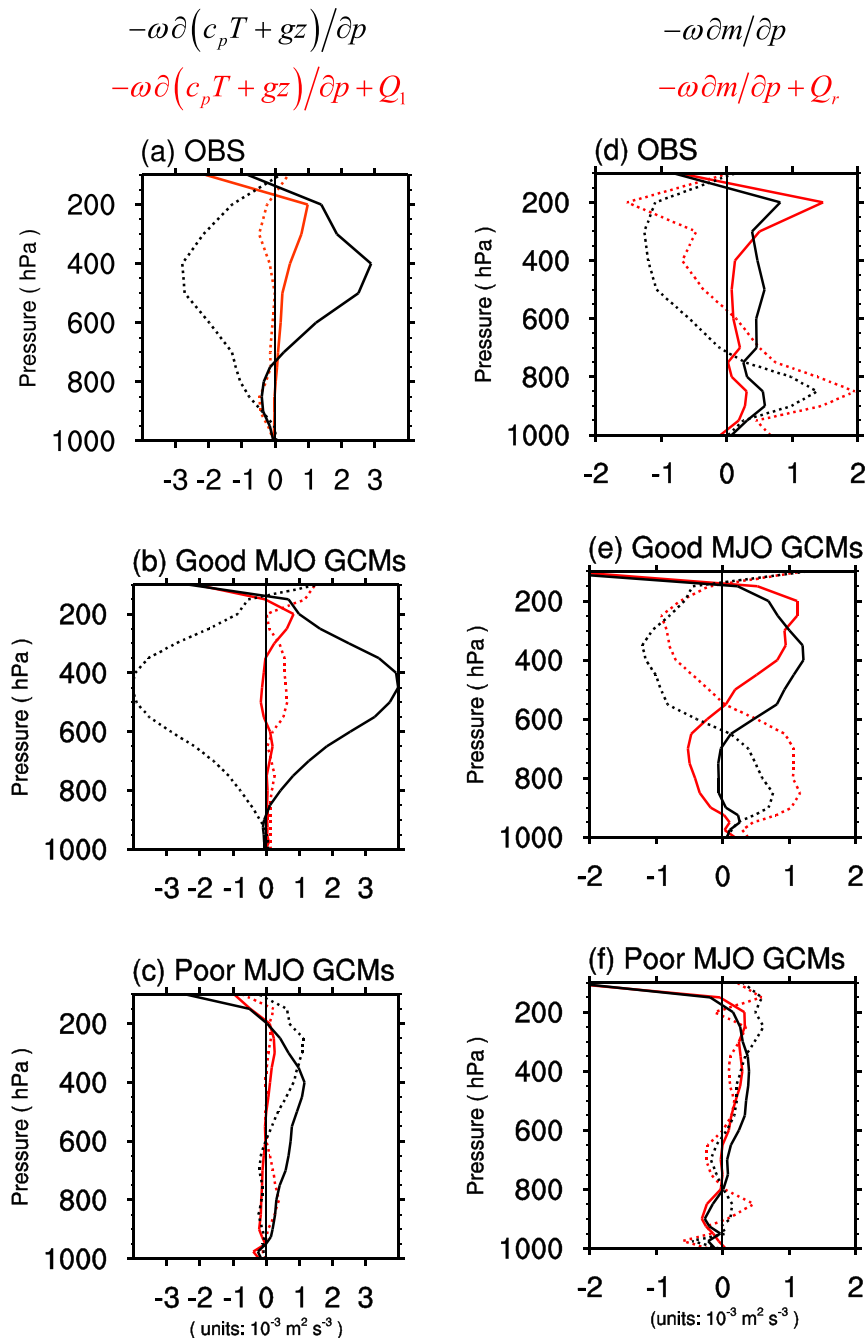
FIG. 20. (a)–(c) Profiles of vertical advection of dry static energy (black) and it plus diabatic heating source (red). (d)–(f) Profiles of vertical advection of MSE (black) and MSE plus atmospheric radiative heating (red), with values derived from (a),(d) reanalysis and (b),(e) the good and (c),(f) poor MJO model composites. Solid lines represent an east box (10°S–10°N, 110°–160°E) average and dashed lines denote a west box (10°S–10°N, 40°–70°E) average.

velocity acting on the mean MSE gradient. As the mean MSE minimizes in the midtroposphere, the second baroclinic mode vertical velocity anomaly to the east and west of the MJO rainfall center could produce a zonally asymmetric MSE tendency. To the east, the downward flow in the upper troposphere and upward flow in the lower troposphere generate a positive MSE tendency; to the west, the upward flow in the upper troposphere and downward flow in the lower troposphere produce a negative MSE tendency. As the

vertical velocity anomaly has a top-heavy structure, the vertical integral of vertical MSE advection is mainly contributed by the upper-level component. The difference between the good and poor model groups is primarily caused by different distributions of intraseasonal vertical velocity anomalies. In the poor group, upper-tropospheric downward flows are seen both to the east and west of the enhanced rainfall region, with maximum amplitude appearing to the west.

Decomposition of horizontal advection into zonal and meridional components reveals that horizontal advection differences between the good and poor models groups are mainly due to the meridional component. Further decomposition shows that meridional moisture advection in the lower free troposphere (600–800 hPa) induced by intraseasonal wind acting on the mean moisture gradient $-v'\partial\overline{q}/\partial y$ is the main contributor. In good group, the winter mean moisture distribution is symmetric about the equator to the east of the enhanced rainfall, and poleward meridional wind anomalies produce a positive MSE tendency. The poleward flow in the lower troposphere is a Rossby wave response to the negative heating anomaly associated with anomalous subsidence. To the west, the mean moisture maximum is confined in Southern Hemisphere, and equatorward meridional wind anomalies in the Northern Hemisphere produce a negative MSE tendency. In the poor group, the Northern Hemispheric poleward flow east of MJO convection and the equatorward flow west of MJO convection are weaker and the mean meridional moisture gradient is also weaker.

Numerical experiments with an aquaplanet model forced by prescribed MJO heating anomalies were conducted to investigate the cause of the key intraseasonal circulation patterns. The simulations show that the presence of stratiform heating in the rear of the MJO convection, rather than the zonal width of the MJO convective region, is responsible for producing the zonal asymmetry of vertical velocity anomalies. It also plays an important role in strengthening the negative heating anomaly to the east and promoting poleward low-level flows. Thus, the lack of stratiform heating in the poor model group is most likely the cause of the nonpropagating intraseasonal mode. These results suggest that realistic representation of the 3D diabatic heating structure associated with the intraseasonal rainfall, especially the stratiform heating in the rear of MJO, is critical in simulating the eastward propagation of the MJO. This result suggests a path forward for parameterization improvement in models to engender an improved MJO simulation.

The role of Rossby wave component in MJO propagation is particularly discussed. Different from previous studies that suggested that a stronger Rossby wave component hinders MJO eastward propagation (Jiang et al. 2015), we found that a stronger Rossby wave component enhances the east–west asymmetry of the MSE tendency and thus favors eastward propagation. The discrepancy lies in the difference of the Rossby wave component between PBL and lower troposphere, and between the north and the south of the equator. Given the observational fact that the maximum horizontal MSE advection anomaly appears in lower troposphere (around 700 hPa) and that the background MSE gradient vanishes south of the equator (around 10°S), one should pay attention to anomalous meridional flow at 700 hPa north of the equator.

The relative roles of zonal and meridional wind components to the east of the MJO convection are also discussed. Different from previous studies that emphasized the Kelvin wave zonal wind component in different propagation behaviors between the good and the poor models (Jiang et al. 2015), we found that the zonal wind induced MSE advection itself does not contribute to different positive MSE tendency to the east; the zonal wind anomaly is a by-product of the enhanced negative heating to the east in association with the stratiform heating in the rear. It is the poleward meridional wind anomaly, which is a Rossby wave response to the negative heating farther east, plays a crucial role. In contrast to pronounced poleward flow in the lower troposphere, boundary layer poleward wind anomaly is much weaker due to boundary layer convergence induced by low pressure anomaly at the top of the PBL (Wang and Li 1994; Hsu and Li 2012).

This study reveals the importance of the vertical MSE advection by second baroclinic mode vertical velocity anomalies in promoting the east–west contrast of MSE tendency. It would be interesting to combine this new mechanism with other propagation mechanisms (e.g., meridional advection, PBL moistening, scale interaction, etc.) in a unified dynamic framework to understand the relative roles of these processes.

REFERENCES

Andersen, J. A., and Z. Kuang, 2012: Moist static energy budget of MJO-like disturbances in the atmosphere of a zonally symmetric aquaplanet. *J. Climate*, **25**, 2782–2804, doi:10.1175/JCLI-D-11-00168.1.

Cai, Q., G. J. Zhang, and T. Zhou, 2013: Impacts of shallow convection on MJO simulation: A moist static energy and moisture budget analysis. *J. Climate*, **26**, 2417–2431, doi:10.1175/JCLI-D-12-00127.1.

Chang, C.-P., and H. Lim, 1988: Kelvin wave-CISK: A possible mechanism for the 30–50 day oscillations. *J. Atmos. Sci.*, **45**, 1709–1720, doi:10.1175/1520-0469(1988)045<1709:KWCAPM>2.0.CO;2.

Chen, L., T. Li, S. K. Behera, and T. Doi, 2016a: Distinctive precursory air–sea signals between regular and super El Niños. *Adv. Atmos. Sci.*, **33**, 996–1004, doi:10.1007/s00376-016-5250-8.

——, Y. Yu, and W. Zheng, 2016b: Improved ENSO simulation from climate system model FGOALS-g1.0 to FGOALS-g2. *Climate Dyn.*, **47**, 2617–2634, doi:10.1007/s00382-016-2988-8.

Dee, D. P., and Coauthors, 2011: The ERA-Interim reanalysis: Configuration and performance of the data assimilation system. *Quart. J. Roy. Meteor. Soc.*, **137**, 553–597, doi:10.1002/qj.828.

Fu, X., and B. Wang, 2009: Critical roles of the stratiform rainfall in sustaining the Madden–Julian oscillation: GCM experiments. *J. Climate*, **22**, 3939–3959, doi:10.1175/2009JCLI2610.1.

Gonzalez, A. O., and X. Jiang, 2017: Winter mean lower tropospheric moisture over the Maritime Continent as a climate model diagnostic metric for the propagation of the Madden-Julian oscillation. *Geophys. Res. Lett.*, **44**, 2588–2596, doi:10.1002/2016GL072430.

Hsu, P.-C., and T. Li, 2012: Role of the boundary layer moisture asymmetry in causing the eastward propagation of the Madden–Julian Oscillation. *J. Climate*, **25**, 4914–4931, doi:10.1175/JCLI-D-11-00310.1.

——, and Y. Yang, 2016: Contribution of atmospheric internal processes to interannual variability of South Asian summer monsoon. *Int. J. Climatol.*, **36**, 2917–2930, doi:10.1002/joc.4528.

——, T. Li, and H. Murakami, 2014: Moisture asymmetry and MJO eastward propagation in an aquaplanet general circulation model. *J. Climate*, **27**, 8747–8760, doi:10.1175/JCLI-D-14-00148.1.

Huffman, G. J., R. F. Adler, M. M. Morrissey, D. T. Bolvin, S. Curtis, R. Joyce, B. McGavock, and J. Susskind, 2001: Global precipitation at one-degree daily resolution from multisatellite observations. *J. Hydrometeor.*, **2**, 36–50, doi:10.1175/1525-7541(2001)002<0036:GPAODD>2.0.CO;2.

Hung, M.-P., J.-L. Lin, W. Wang, D. Kim, T. Shinoda, and S. J. Weaver, 2013: MJO and convectively coupled equatorial waves simulated by CMIP5 climate models. *J. Climate*, **26**, 6185–6214, doi:10.1175/JCLI-D-12-00541.1.

Jiang, X., 2017: Key processes for the eastward propagation of the Madden–Julian oscillation based on multi-model simulations. *J. Geophys. Res. Atmos.*, **122**, 755–770, doi:10.1002/2016JD025955.

——, and Coauthors, 2015: Vertical structure and physical processes of the Madden–Julian oscillation: Exploring key model physics in climate simulations. *J. Geophys. Res. Atmos.*, **120**, 4718–4748, doi:10.1002/2014JD022375.

Johnson, R. H., T. M. Rickenbach, S. A. Rutledge, P. E. Ciesielski, and W. H. Schubert, 1999: Trimodal characteristics of tropical convection. *J. Climate*, **12**, 2397–2418, doi:10.1175/1520-0442(1999)012<2397:TCOTC>2.0.CO;2.

Kessler, W. S., and R. Kleeman, 2000: Rectification of the Madden–Julian oscillation into the ENSO cycle. *J. Climate*, **13**, 3560–3575, doi:10.1175/1520-0442(2000)013<3560:ROTMJO>2.0.CO;2.

Kim, D., and Coauthors, 2009: Application of MJO simulation diagnostics to climate models. *J. Climate*, **22**, 6413–6436, doi:10.1175/2009JCLI3063.1.

——, A. H. Sobel, E. D. Maloney, D. M. W. Frierson, and I.-S. Kang, 2011: A systematic relationship between intraseasonal variability and mean state bias in AGCM simulations. *J. Climate*, **24**, 5506–5520, doi:10.1175/2011JCLI4177.1.

——, J.-S. Kug, and A. H. Sobel, 2014: Propagating versus nonpropagating Madden–Julian oscillation events. *J. Climate*, **27**, 111–125, doi:10.1175/JCLI-D-13-00084.1.

Kiranmayi, L. and E. D. Maloney, 2011: Intraseasonal moist static energy budget in reanalysis data. *J. Geophys. Res.*, **116**, D21117, doi:10.1029/2011JD016031.

Kuang, Z., 2008: A moisture-stratiform instability for convectively coupled waves. *J. Atmos. Sci.*, **65**, 834–854, doi:10.1175/2007JAS2444.1.

Lau, K.-M., and P. H. Chan, 1986: Aspects of the 40–50 day oscillation during the northern summer as inferred from outgoing longwave radiation. *Mon. Wea. Rev.*, **114**, 1354–1367, doi:10.1175/1520-0493(1986)114<1354:AOTDOD>2.0.CO;2.

——, and L. Peng, 1987: Origin of low-frequency (intraseasonal) oscillations in the tropical atmosphere. Part I: Basic theory. *J. Atmos. Sci.*, **44**, 950–972, doi:10.1175/1520-0469(1987)044<0950:OOLFOI>2.0.CO;2.

Liebmann, B., H. H. Hendon, and J. D. Glick, 1994: The relationship between tropical cyclones of the western Pacific and Indian Oceans and the Madden–Julian oscillation. *J. Meteor. Soc. Japan*, **72**, 401–412.

Lin, J., B. Mapes, M. Zhang, and M. Newman, 2004: Stratiform precipitation, vertical heating profiles, and the Madden–Julian oscillation. *J. Atmos. Sci.*, **61**, 296–309, doi:10.1175/1520-0469(2004)061<0296:SPVHPA>2.0.CO;2.

——, and Coauthors, 2006: Tropical intraseasonal variability in 14 IPCC AR4 climate models. Part I: Convective signals. *J. Climate*, **19**, 2665–2690, doi:10.1175/JCLI3735.1.

Liu, F., and B. Wang, 2012: A frictional skeleton model for the Madden–Julian oscillation. *J. Atmos. Sci.*, **69**, 2749–2758, doi:10.1175/JAS-D-12-020.1.

——, and ——, 2016: Role of horizontal advection of seasonal-mean moisture in the Madden–Julian oscillation: A theoretical model analysis. *J. Climate*, **29**, 6277–6293, doi:10.1175/JCLI-D-16-0078.1.

Madden, R. A., and P. R. Julian, 1972: Description of global-scale circulation cells in the tropics with a 40–50 day period. *J. Atmos. Sci.*, **29**, 1109–1123, doi:10.1175/1520-0469(1972)029<1109:DOGSCC>2.0.CO;2.

Majda, A. J., S. N. Stechmann, and B. Khouider, 2007: Madden–Julian Oscillation analog and intraseasonal variability in a multicloud model above the equator. *Proc. Natl. Acad. Sci. USA*, **104**, 9919–9924, doi:10.1073/pnas.0703572104.

Maloney, E. D., 2009: The moist static energy budget of a composite tropical intraseasonal oscillation in a climate model. *J. Climate*, **22**, 711–729, doi:10.1175/2008JCLI2542.1.

Mapes, B. E., 2000: Convective inhibition, subgrid-scale triggering energy, and stratiform instability in a toy tropical wave model. *J. Atmos. Sci.*, **57**, 1515–1535, doi:10.1175/1520-0469(2000)057<1515:CISSTE>2.0.CO;2.

Medeiros, B., B. Stevens, I. M. Held, M. Zhao, D. L. Williamson, J. G. Olson, and C. S. Bretherton, 2008: Aquaplanets, climate

sensitivity, and low clouds. *J. Climate*, **21**, 4974–4991, doi:10.1175/2008JCLI1995.1.

Murakami, T., and T. Nakazawa, 1985: Tropical 45 day oscillations during the 1979 Northern Hemisphere summer. *J. Atmos. Sci.*, **42**, 1107–1122, doi:10.1175/1520-0469(1985)042<1107:TDODTN>2.0.CO;2.

Neelin, J. D., and I. M. Held, 1987: Modeling tropical convergence based on the moist static energy budget. *Mon. Wea. Rev.*, **115**, 3–12, doi:10.1175/1520-0493(1987)115<0003:MTCBOT>2.0.CO;2.

——, and J.-Y. Yu, 1994: Modes of tropical variability under convective adjustment and the Madden–Julian oscillation. Part I: Analytical theory. *J. Atmos. Sci.*, **51**, 1876–1894, doi:10.1175/1520-0469(1994)051<1876:MOTVUC>2.0.CO;2.

Petch, J., D. Waliser, X. Jiang, P. K. Xavier, and S. Woolnough, 2011: A global model inter-comparison of the physical processes associated with the MJO. *GEWEX News*, August 2011, International GEWEX Project Office, Silver Spring, MD, 3–5.

Raymond, D. J., 2000: Thermodynamic control of tropical rainfall. *Quart. J. Roy. Meteor. Soc.*, **126**, 889–898, doi:10.1002/qj.49712656406.

——, 2001: A new model of the Madden–Julian oscillation. *J. Atmos. Sci.*, **58**, 2807–2819, doi:10.1175/1520-0469(2001)058<2807:ANMOTM>2.0.CO;2.

Reynolds, R. W., N. A. Rayner, T. M. Smith, D. C. Stokes, and W. Wang, 2002: An improved in situ and satellite SST analysis for climate. *J. Climate*, **15**, 1609–1625, doi:10.1175/1520-0442(2002)015<1609:AIISAS>2.0.CO;2.

Rienecker, M. M., and Coauthors, 2011: MERRA: NASA's Modern-Era Retrospective Analysis for Research and Applications. *J. Climate*, **24**, 3624–3648, doi:10.1175/JCLI-D-11-00015.1.

Roeckner, E., and Coauthors, 1996: The atmospheric general circulation model ECHAM-4: Model description and simulation of present-day climate. Max-Planck-Institut für Meteorologie Rep. 218, 90 pp. [Available online at www.mpimet.mpg.de/fileadmin/publikationen/Reports/MPI-Report_218.pdf.]

Russell, D. R., 2006: Development of a time-domain, variable-period surface-wave magnitude measurement procedure for application at regional and teleseismic distances. Part I: Theory. *Bull. Seismol. Soc. Amer.*, **96**, 665–677, doi:10.1785/0120050055.

Schiro, K. A., J. D. Neelin, D. K. Adams, and B. R. Lintner, 2016: Deep convection and column water vapor over tropical land vs. tropical ocean: A comparison between the Amazon and the tropical western Pacific. *J. Atmos. Sci.*, **73**, 4043–4063, doi:10.1175/JAS-D-16-0119.1.

Slingo, J., and Coauthors, 1996: Intraseasonal oscillations in 15 atmospheric general circulation models: Results from an AMIP diagnostic subproject. *Climate Dyn.*, **12**, 325–357, doi:10.1007/BF00231106.

Sobel, A. and E. Maloney, 2012: An idealized semi-empirical framework for modeling the Madden–Julian oscillation. *J. Atmos. Sci.*, **69**, 1691–1705, doi:10.1175/JAS-D-11-0118.1.

——, and ——, 2013: Moisture modes and the eastward propagation of the MJO. *J. Atmos. Sci.*, **70**, 187–192, doi:10.1175/JAS-D-12-0189.1.

——, J. Nilsson and L. M. Polvani, 2001: The weak temperature gradient approximation and balanced tropical moisture waves. *J. Atmos. Sci.*, **58**, 3650–3665, doi:10.1175/1520-0469(2001)058<3650:TWTGAA>2.0.CO;2.

——, S. Wang, and D. Kim, 2014: Moist static energy budget of the MJO during DYNAMO. *J. Atmos. Sci.*, **71**, 4276–4291, doi:10.1175/JAS-D-14-0052.1.

Wang, B., 1988: Dynamics of tropical low-frequency waves: An analysis of the moist Kelvin wave. *J. Atmos. Sci.*, **45**, 2051–2065, doi:10.1175/1520-0469(1988)045<2051:DOTLFW>2.0.CO;2.

——, and H. Rui, 1990: Synoptic climatology of transient tropical intraseasonal convection anomalies: 1975–1985. *Meteor. Atmos. Phys.*, **44**, 43–61, doi:10.1007/BF01026810.

——, and T. Li, 1994: Convective interaction with boundary-layer dynamics in the development of a tropical intraseasonal system. *J. Atmos. Sci.*, **51**, 1386–1400, doi:10.1175/1520-0469(1994)051<1386:CIWBLD>2.0.CO;2.

Wang, L., and T. Li, 2017: Roles of convective heating and boundary-layer moisture asymmetry in slowing down the convectively coupled Kelvin waves. *Climate Dyn.*, **48**, 2453–2469, doi:10.1007/s00382-016-3215-3.

Weickmann, K. M., 1983: Intraseasonal circulation and outgoing longwave radiation modes during Northern Hemisphere winter. *Mon. Wea. Rev.*, **111**, 1838–1858, doi:10.1175/1520-0493(1983)111<1838:ICAOLR>2.0.CO;2.

Wheeler, M. and J. McBride, 2005: Australian–Indonesian monsoon. *Intraseasonal Variability in the Atmosphere–Ocean Climate System*, W. Lau and D. Waliser, Eds., Springer, 125–173.

Xiang, B., B. Wang, A. Lauer, J.-Y. Lee, and Q. Ding, 2014: Upper tropospheric warming intensifies sea surface warming. *Climate Dyn.*, **43**, 259–270, doi:10.1007/s00382-013-1928-0.

Yanai, M., S. Esbensen, and J.-H. Chu, 1973: Determination of bulk properties of tropical cloud clusters from large-scale heat and moisture budgets. *J. Atmos. Sci.*, **30**, 611–627, doi:10.1175/1520-0469(1973)030<0611:DOBPOT>2.0.CO;2.

Yasunari, T., 1979: Cloudiness fluctuations associated with the Northern Hemisphere summer monsoon. *J. Meteor. Soc. Japan*, **57**, 227–242.